Exploring Possible Spatial-Frequency-Tuned Channels by Measurement of Impulse Responses

Lin SHI

Graduate School of Engineering

Kochi University of Technology

A dissertation submitted for the degree of

Doctor of Engineering

February 2013

Summary

The spatial information processing is an essential aspect in human vision while the fundamental questions about spatial-frequency-tuned channels remain controversial. In this dissertation, the impulse responses of double-pulse detection using various spatial structure stimuli with separate positive- and negative-contrast and using stimuli with ring-structure Fourier spectrum at different spatial frequencies were studied to explore the possible spatial-frequency-tuned channels through the impulse response function (IRF) which was psychophysically measured by the double-pulse detection threshold through the working model and characterized a time-invariant linear system completely.

Firstly, in the first experiment, double-pulse thresholds and IRFs of the positive- and negative- contrast detection by separated positive- and negative-contrast stimuli with various circular spatial structures were measured. The purpose is to explore the possible spatial-frequency-tuned channels and to investigate the temporal characteristics and sensitivities of the positive- and negative-contrast detection. Because whether positive- and negative-contrast sensitivities are the same is a fundamental issue of visual processing.

Results showed that the impulse responses of positive- and negative-

contrast detection were similar except the maximum amplitude of the first phase which concerned with the sensitivity of contrast detection. It is simply reflecting that sensitivity of positive contrast detection was lower than that of negative contrast detection. The different sensitivity of positive- and negative-contrast detection can be originated from the summation part instead of the linear filter part of visual system according to the working model of human vision.

Although a new attempt was tried with use of stimuli with ring-structure Fourier spectrum, however, the attempt to investigating impulse responses of the possible spatial-frequency-tuned channels failed because the strong very low spatial frequency component dominated the Fourier spectrum of the various spatial structure stimuli, because those had to be used for the measurement of the positive- and negative-contrast experiment.

Secondly, in the second experiment, double-pulse thresholds of contrast detection using stimuli with ring-structure Fourier spectrum at different spatial frequencies were measured psychophysically on human observers in order to get IRFs and then to investigate the impulse responses and the sensitivities of the possible spatial-frequency-tuned channels.

Results showed that: (1) the double-pulse detection thresholds of lower spatial frequencies (1 and 2 cycle per degree (cpd)) were lower than those of higher spatial frequencies (8 and 16 cpd), and (2) IRFs of lower spatial frequencies (1 and 2 cpd) were significantly differ-

ent with IRFs of higher spatial frequencies (8 and 16 cpd) both on the phase, the first zero-crossing time, and the amplitude. The IRFs of lower spatial frequencies had two or three phases while those of higher spatial frequencies had only one phase (except one observer had a very weak second phase). The first zero-crossing time of IRFs of lower spatial frequencies were shorter and the amplitude of IRFs of lower spatial frequencies were higher, compared to those of higher spatial frequencies. (3) The peak frequency of temporal contrast sensitivity function (tCSF) derived from IRFs was higher in lower spatial frequencies (1 and 2 cpd) than that in higher spatial frequencies (8 and 16 cpd).

Above results indicated that at least two kinds of spatial-frequency-tuned channels, the lower- and higher-spatial-frequency-tuned channels that dominate the detection of lower spatial frequencies (0, 1, and 2 cpd) and the detection of high spatial frequencies (8 and 16 cpd), respectively, exists in human vision. The lower-spatial-frequency-tuned channel is bandpass and the higher-spatial-frequency-tuned channel is low-pass. However, the accurate number of spatial-frequency-tuned channels could not be estimated because of the possible limit of measurement with the double pulse method for the IRF that is using the detection threshold.

These results in the present study were discussed with physiological consideration which supported that the M- and P-pathways in human visual system dominated the detection of the lower spatial frequencies

(0, 1, and 2 cpd) and the higher spatial frequencies (8 and 16 cpd), respectively, in the present study.

The different impulse responses between the M- and P-pathways and the difference between spatial frequency and spatial structure were also discussed.

Five chapters are included in this dissertation. Chapter 1 introduces the background knowledge about the temporal sensitivity, the working model of temporal sensitivity, the IRF, the estimation of IRF, the double-pulse method, the staircase method, and the psi method.

Chapter 2 is about impulse responses and sensitivities of positive- and negative-contrast detection. IRFs and double-pulse thresholds of positive- and negative-contrast detection with various circular spatial structure stimuli were measured to investigate the temporal characteristics and sensitivities of positive- and negative-contrast detection. Introduction section reviews conflicting results about sensitivities of the positive- and negative-contrast detection measured by various investigators. Method section describes the stimuli, the log contrast energy threshold, apparatus, calibration of CRT, procedure, estimation of IRFs, and statistical analysis of the experiment. Results section shows results of the positive- and negative-contrast detection thresholds of double-pulse detection, the comparison of positive- and negative-contrast thresholds, IRFs of positive- and negative-contrast detection, the paired comparison of positive- and negative-contrast IRFs, and the distributions of peak times and amplitude of IRFs. Dis-

cussion and Conclusion sections as described above. Appendix section shows the comparison of calculated IRFs between two models.

Chapter 3 is about impulse responses of the possible spatial-frequency-tuned channels. IRFs and double-pulse thresholds of contrast detection of stimuli with ring-structure of Fourier spectrum at different spatial frequencies were measured to investigate the temporal characteristics of the possible spatial-frequency-tuned channels. Introduction section reviews the possible spatial-frequency-tuned channels. Method section describes the stimuli, the log contrast energy threshold, apparatus, calibration of CRT, procedure, and estimation of IRFs in the experiment. Results section shows results about IRFs of spatial frequency 1, 2, 4, 8, and 16 cpd, the peak time and the amplitude of IRFs, the double-pulse detection thresholds, and temporal contrast sensitivity functions derived from IRFs. Discussion and Conclusion sections as described above with motion models concerned with impulse responses.

Chapter 4 includes experimental techniques; estimating of the psychometric function using the extreme value distribution function, the display model for calibration, the comparison of the staircase method and the psi method, an introduction of the Fourier-spectrum contrast, and the contrast variation simulation of eye movements. A reverse form of the extreme value distribution function is derived to estimate the psychometric function of contrast detection. A display model that can get less than 3% display error rate of the CIE 1931

luminance and chromatic coordinate on a CRT monitor is introduced for the accurate calibration. The comparison of the staircase and psi methods shows that both methods can get similar thresholds while the psi method is more efficient than the staircase method in the present study. The simulation results showed that the positive- and negative-contrast stimuli and the spatial frequency stimuli used in this study are better than the Gabor stimuli in term of the contrast variation caused by the eye movement during the double pulses.

Chapter 5 summarizes the conclusions of this dissertation.

Contents

List of Figures

LIST OF FIGURES

List of Tables

Chapter 1

Background

This chapter introduces brief background knowledge about the temporal sensitivity, the working model of temporal sensitivity, the IRF, the estimation of IRF, the double-pulse method, the staircase method, and the psi method.

1.1 The temporal sensitivity

The temporal sensitivity is an important aspect of human vision. The importance related to the requirement of dynamic visual information capture. The temporal sensitivity was investigated through various stimuli varying over time in different ways, for example, sinusoids, rectangular pulses, and double-pulse.

In general form, the stimulation can be described as a function of spatial and temporal argument as following equation.

$$S(x, y, t) = S_t(x, y)$$

$S(x, y, t)$ is the stimulation of two dimension space point (x, y) at time point t,

S_t the function of a two dimension space stimulation (x, y) vary over time t. In other words, the stimulation is a sequential spatial distribution which vary over time.

The response of human vision system can be simplified as Equation 1.1 without consideration of other factors rather than spatial and temporal factor, x, y, and t.

$$R = V(S(x, y, t)) \tag{1.1}$$

The purpose of the visual psychophysics research is to identify the relationship V between the stimulation S and the response R.

The stimulation can be simplified as

$$S(x, y, t) = S_{sp}(x, y)S_{tp}(t)$$

when the spatial distribution S_{sp} dose not vary over time. In other words, the one dimension control variable S_{tp} is what I am interested in while the spatial distribution dose not vary over time.

In most cases, V can not be described as a linear system. But, it can be simplified as a linear system or can be decomposed as a linear system followed by a non-linear system. In this case, the Linear Systems Theory will be a powerful tool. Indeed, the Linear Systems Theory had played a key role in the investigation of temporal sensitivity [Watson, 1986].

Following content introduces a working model which can explain many aspects of temporal sensitivity and is composed by a linear filter followed by a non-linear summation process.

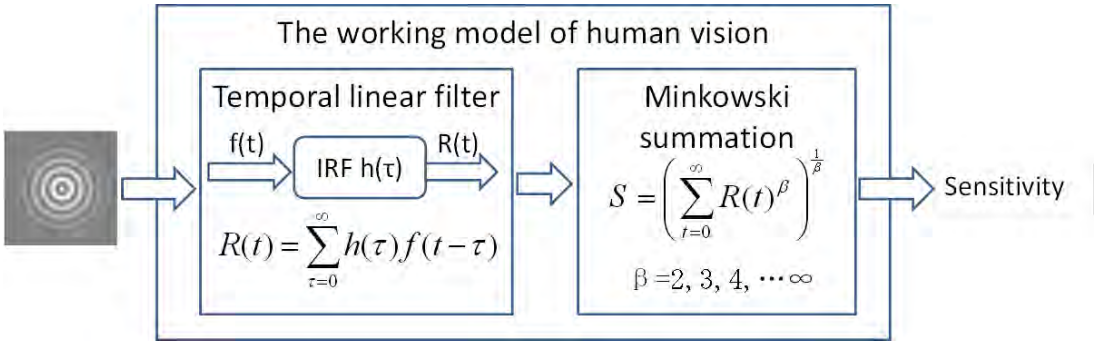

Figure 1.1: The working model. A temporal linear filter is followed by a Minkowski summation. The model input is the stimuli varied over time and the model output is the sensitivity. $f(t)$ is the input of the linear filter. $h(\tau)$ is the IRF. $R(t)$ is the internal response. β is the factor of summation. S is the sensitivity.

1.2 The working model

Temporal sensitivities in many kinds of stimuli were explained by a generic model which was called as 'a working model' [Watson, 1986]. The working model included a linear filter followed by a probability summation over time (see Figure 1.1). In Watson's later model [Watson and Ahumada, 2005], a more general summation, Minkowski summation, was used. Characteristics of the linear filter were investigated by estimating the impulse response function (IRF) or the temporal transfer function of the filter.

The first part of the working model is a linear system which is described by the impulse response function as following equation.

$$R(t) = \sum_{t=0}^{\infty} h(\tau) f(t-\tau)$$

$R(t)$ is the output of the system, $f(t)$ the input of the system, $h(t)$ the impulse response function or the weight function. This equation is the definition of linear

system. The output $R(t)$ is the weight-summation of history input $f(t-\tau)$.

The second part of the working model is a Minkowski summation described as follow equation.

$$S = \left(\sum_{t=0}^{\infty} R(t)^{\beta} \right)^{\frac{1}{\beta}}$$

S is the sensitivity, $R(t)$ the output of the linear system, β factor of the summation.

A linear system can be identified completely by the impulse response function $h(t)$ or the transform function $G(q)$. The transform function is defined as following equation.

$$G(q) = \sum_{k=1}^{\infty} h(k) q^{-k}$$

$G(q)$ is the transform function, $h(k)$ the impulse response function, q the forward shift operator by

$$qf(t) = f(t+1)$$

and the backward shift operator q^{-1}

$$q^{-1} f(t) = f(t-1)$$

The linear system can be expressed as following equation by the transform function.

$$R(t) = G(q) f(t)$$

As described before, the purpose of the psychophysical investigation is to explore the characteristics of the relationship V in Equation 1.1 which is identified by the impulse response function or the transform function of the first part of

the working model and the summation factor β of the second part of the working model. So, the key task is to the estimate the impulse response function which is introduced as following.

1.3 Impulse response function

The impulse response function (IRF) is also called as the weighting function, which is a linear weighting of sequential inputs and characterizes a time-invariant linear system completely. It can be used to predict response to any temporally modulated response, theoretically.

In mathematics, the impulse response function is a weight of the history input described as following equation.

$$R(t) = \sum_{t=0}^{\infty} h(\tau) f(t - \tau)$$

$R(t)$ is the output of the system, $f(t)$ the input of the system, $h(t)$ the impulse response function.

In psychophysical investigation, IRFs have been obtained for various purposes. IRFs were calculated from transfer functions by the Fourier transform under various luminance conditions [Kelly, 1961, 1971] and by reconstructing the temporal phase spectrum [Stork and Falk, 1987]. From temporal summation index of positive and negative flashes, hypothetical IRFs of positive and negative flashes were obtained [Ikeda, 1965]. Chromatic IRFs as the responses of red, green, yellow, or blue flashes were also measured [Uchikawa and Ikeda, 1986; Uchikawa and Yoshizawa, 1993]. Burr and Morrone [Burr and Morrone, 1993] provided a new

model set to estimate IRF and measured chromatic and achromatic IRFs. Later, they measured IRFs during saccades [Burr and Morrone, 1996]. Shinomori and Werner investigated senescence of IRFs [Shinomori and Werner, 2003], IRFs of S-cone pathways [Shinomori and Werner, 2006, 2008], and aging of human S-cone pathways [Shinomori and Werner, 2012]. Additionally, reaction time could be estimated by a model based on IRF [Cao et al., 2007].

The impulse response function is estimated psychophysically from sequential double-pulse detection thresholds which were divided by various inter-stimuli-interval (ISI). The double-pulse method and the estimation method are described as following.

1.4 Double-pulse method

The double-pulse method includes two same pulses divided by an inter-stimuli-interval (ISI) which only displays the background. The duration of the pulse need to be short enough. In this study, the duration of the pulse was 6.7 msec (1 frame) which is the minimum value using a CRT display at 150 Hz frame rate.

The intensity of double-pulse was measured by the intensity of single pulse while the intensities of two pulses were the same in this study.

Figure 1.2 showed the frame sequence of the double-pulse used in this study.

The double-pulse detection threshold is the intensity value of the double-pulse which observer can detect the stimuli from background in a certain probability.

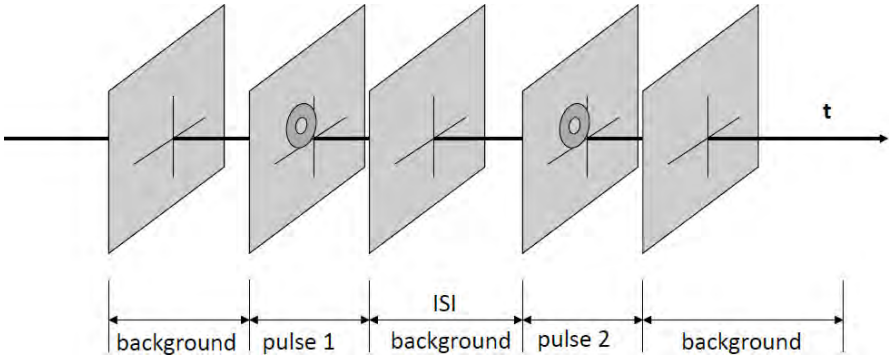

Figure 1.2: The double-pulse method. Gray rectangles indicate frames displayed on the CRT display in one trial of the double-pulse method. From the left to the right, the 1st, 3rd, and 5th frames are background frames and the 2nd and 4th frames are stimulus frames which include the stimulus images. The first pulse begins from the 2nd frame and ends at the 3rd frame. The second pulse begins from the 4th frame and ends at the 5th frame. The pulse one and the pulse two are totally same. Other frames display background only. The temporal interval marked as ISI is the inter-stimuli-interval.

1.5 Estimation of IRF

In the field of electric engineering, the IRF can be obtained directly by measuring the response of a system to a pulse-input with very huge intensity and very tiny duration. For human vision channels, IRFs can be estimated from double-pulses thresholds using the working model [Watson, 1986, 1979] with both Watson's model set [Watson, 1986] and Burr and Morrone's model set [Burr and Morrone, 1993].

The estimation of IRF is a reverse procedure of the working model. In other words, the estimation procedure is to get the IRF from the sequential thresholds which were corresponding with various ISI setting of a double-pulse method. In mathematics, this procedure was called as the system identification. The purpose of the system identification is to get the model parameters of system through controlling input of the system and obtaining output of the system. In

the experiments of this dissertation, the input variable is the ISI and the output value is the threshold.

According to the working model, the threshold can be expressed as following equation.

$$C^{-1} = \left(\sum_i \left| \sum_j f_j h_{i-j} \right|^{\beta} \right)^{\frac{1}{\beta}} \tag{1.2}$$

In Equation 1.2, C was the contrast at threshold. C^{-1} was the Minkowski summation of the convolution of input f and IRF h. Following Shinomori [Shinomori and Werner, 2003], β was set to 4.

The IRF shape can be expressed mathematically using various elementary functions with corresponding parameters. There are two kinds of expression of IRF shapes. One is using the sinusoidal function proposed by Burr and Morrine (see equation 1.3) and the other is using the exponential function proposed by Watson (see equations 1.4, 1.5, and 1.6).

Burr and Morrine's model set [Burr and Morrone, 1993] was expressed as Equation 1.3. It had 4 parameters, a_0, a_1, a_2 and a_3. Parameter, a_0 was the overall gain of the function. Parameter, a_1 was the fundamental frequency of oscillation. Parameter, a_2 was the modulation of frequency over time. Parameter, a_3 was the steepness of the exponential decay.

$$h(t) = a_0 u(t) t \sin\{2\pi[a_1 t(t+1)^{-a_2}]\} e^{-a_3 t} \tag{1.3}$$

In Watson's model set [Watson, 1986], the IRF was expressed as Equations

1.4, 1.5, and 1.6.

$$h(t) = \xi[h_1(t) - \zeta h_2(t)] \tag{1.4}$$

$$h_1(t) = u(t)[\tau(n_1 - 1)!]^{-1}(t/\tau)^{n_1-1}e^{-t/\tau} \tag{1.5}$$

$$h_2(t) = u(t)[k\tau(n_2 - 1)!]^{-1}(t/(k\tau))^{n_2-1}e^{-t/(k\tau)} \tag{1.6}$$

There were 4 parameters, ξ, ζ, τ, and k (n_1 was set to 3 and n_2 was set to 5). Parameters, ξ and ζ were weighting values of two components. Parameter, τ was time constant. Parameter, k was the time constant ratio. $u(t)$ was the unit step function.

Those model-parameters were estimated by a nonlinear regression analysis procedure with a least-square method. I practically used $nlinfit$ function in the statistics toolbox of Matlab. Millenary initial parameters were generated randomly to try to cover possible shape of IRFs. Because the calculated IRFs from these models were similar (See the following section for details), IRFs only from Burr and Morrone's model were presented in this dissertation.

1.6 The staircase and psi method

Threshold is an important basic measurement in psychophysics. The threshold values are estimated through a procedure included serial trials. The staircase method and the psi method are introduced in the following content.

1.6.1 The staircase method

The staircase method is a classic method to measure threshold. The two-down-one-up (2d1u) staircase method is introduced here. From an initial intensity value above the pre-set threshold value, decrease the intensity value of stimulus with certain step after two correct answers and increase the intensity value after one incorrect answer. The step is usually big at initial trials and is small at later trials. The point where the intensity changes direction is called the turning point (see Figure 1.3). After achieving a certain number (e.g. 6) of turning point, the procedure will finish. The estimated threshold value is the mean of last four turning point.

1.6.2 The psi method

The psi method proposed by Kontsevich and Tyler [Kontsevich and Tyler, 1999]. The principle of the psi method is to maximize the entropy gathered from trials. The psi method needs to set the initial distribution of thresholds and slopes. The psi method can estimate the threshold and slope at the same time. A typical psi procedure was displayed in Figure 1.4. Prins and Kingdom's implementation [Prins and Kingdom, 2009] of the psi method was used in this dissertation.

The psi method estimated the threshold and the slope values adaptively through a 2-dimension distribution of those two parameters. An initial distribution was set as a prior distribution of the threshold and the slope before the beginning of a psi procedure. After each trial, the prior distribution was updated dynamically using the observer's response. The strategy for placing the new trial was to choose the one that leads to the smallest expected entropy one step ahead

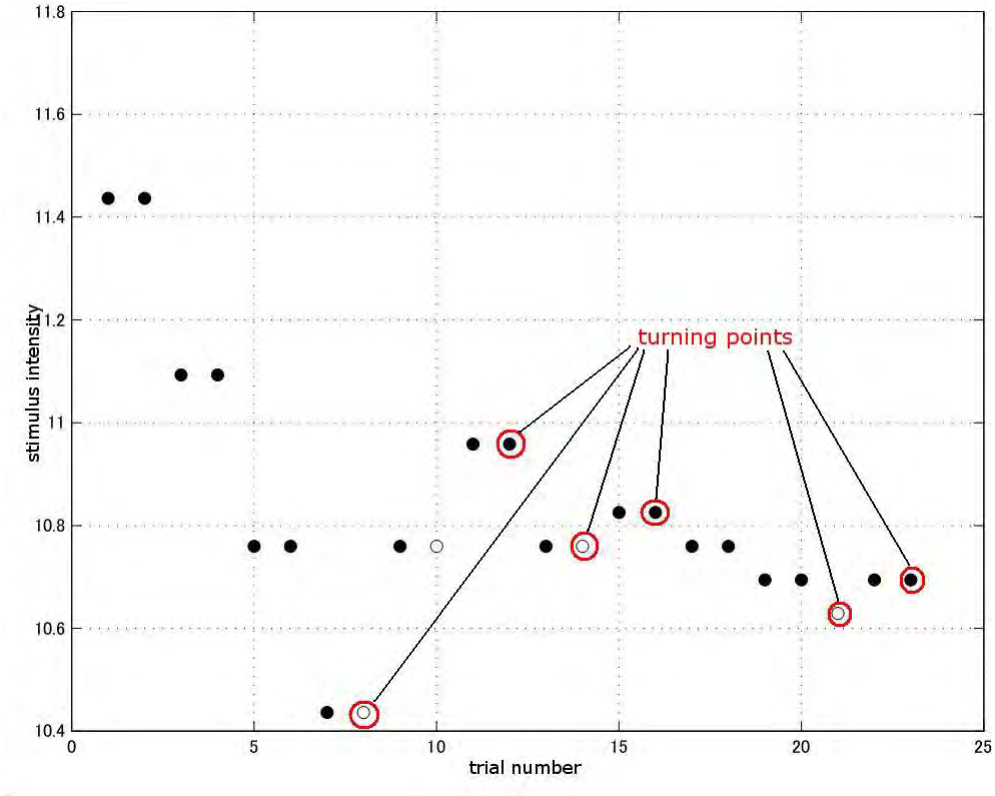

Figure 1.3: The staircase procedure. The abscissa is the number of trials and the ordinate is the intensity of stimulus. The filled circles indicate correct answers and the empty circles indicate incorrect answers. Points marked by red circles are the turning points.

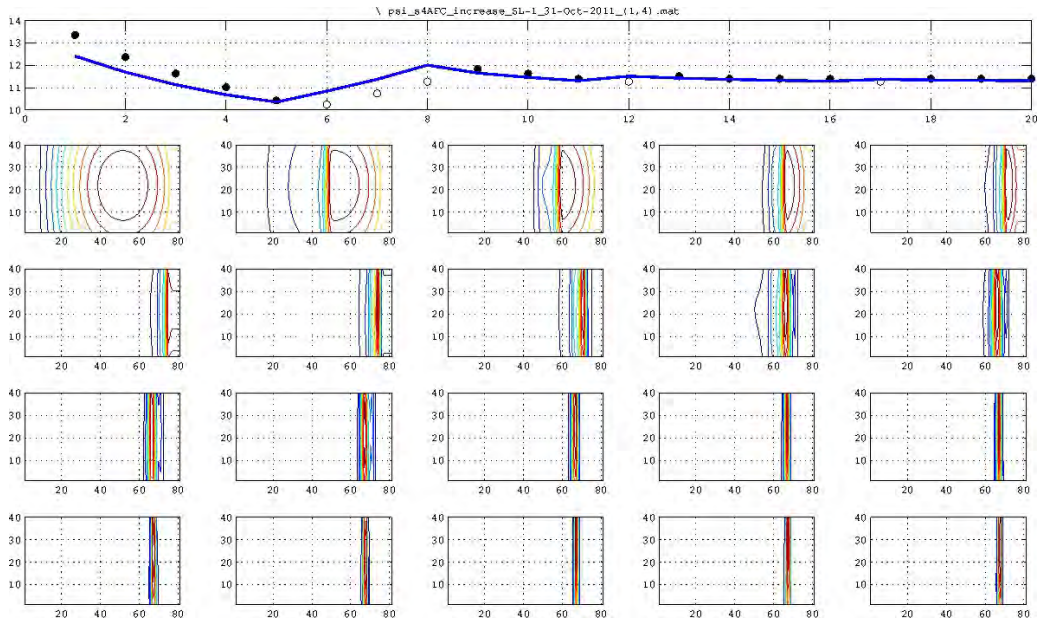

Figure 1.4: The psi procedure. The top panel shows the intensity of 20 trials. The abscissa is the number of trials and the ordinate is the intensity of stimulus. The filled circles indicate correct answers and the empty circles indicate incorrect answers. The blue line indicates the estimated thresholds after each trial. The other panels show the distributions of thresholds and slopes. The abscissa is the threshold and the ordinate is the slope.

Kontsevich and Tyler [1999], H_{t+1}.

$$H_{t+1} = -\sum_{\lambda} p_t(\lambda) log(p_t(\lambda))$$

λ was a vector of threshold and slope, $p_t(\lambda)$ was the probabilities that reflect the chance for the psychometric function with parameter λ to match the actual psychometric function. The intensity of the next trial was decided by maximizing the information gathered from observer's responses. The psi process stopped when the number of trials was bigger than a pre-setting-value.

A comparison between the staircase method and the psi method is showed in Chapter 4. In this dissertation, the psi method was used to control the intensity of stimuli in various trials. The thresholds were calculated as the average value of the last four turning-points.

Chapter 2

IRFs of Positive- and Negative-Contrast Detection

In this chapter, double-pulse thresholds and IRFs of the positive- and negative-contrast detection by separated positive- and negative-contrast stimuli with various circular spatial structures were measured. The purpose is to explore the possible spatial-frequency-tuned channels and to investigate the temporal characteristics and sensitivities of the positive- and negative-contrast detection. Because whether positive- and negative-contrast sensitivities are the same is a fundamental issue of visual processing.

Results showed that the impulse responses of positive- and negative-contrast detection were similar except the maximum amplitude of the first phase which concerned with the sensitivity of contrast detection. It is simply reflecting that sensitivity of positive contrast detection was lower than that of negative contrast detection. The different sensitivity of positive- and negative-contrast detection can be originated from the summation part instead of the linear filter part of

visual system according to the working model of human vision.

2.1 Introduction

It has been a basic psychophysical issue whether positive- and negative-contrast sensitivities are the same [Bowen et al., 1989]. In previous literature, conflicting results have been reported in various experimental conditions by different investigators. Boynton, Ikeda, and Stiles reported that a decrement threshold was lower than an increment threshold in the case of using red increment or decrement upon green background [Boynton et al., 1964]. Short also reported similar results under a low background luminance condition [Short, 1966]. Patel and Jones found that the increment threshold was consistently greater than the decrement threshold [Patel and Jones, 1968]. Bowen et al. reported more sensitive to decrements than increments using saw-tooth contrast stimulation [Bowen et al., 1989]. However, Herrick [Herrick, 1956] and Rashbass [Rashbass, 1970] found little difference between increments and decrements. Watson and Nachmias found positive thresholds were equal with negative ones using grating targets [Watson and Nachmias, 1977]. These reports about increments and decrements were studied in terms of temporal sensitivity.

In this study, I tried to investigate the positive- and negative-contrast sensitivities with double-pulse method using various spatial structure stimuli. Firstly, the detection thresholds of double pulses were compared between positive- and negative-contrast stimuli. Secondly, the IRFs that were estimated from sequential double-pulse detection thresholds were also be compared to investigate the temporal characteristics of positive- and negative-contrast detection.

Results indicated that, positive contrast detection thresholds were significantly higher than negative contrast detection thresholds. However, there was no significant difference at three conditions on one observer and four conditions on another one observer in all six conditions on five observers. This individual difference can be one of reasons why conflictive results have been reported in previous literature. Moreover, the results showed that in terms of temporal characteristics, the IRFs of positive contrast were similar to the IRFs of negative contrast. According to the working model, the possible source of different sensitivity is the summation part while the temporal linear filter part was similar. The slope values of positive contrast detection were significantly different with those of negative contrast detection except one observer and it supports that the source of different sensitivities between positive- and negative-contrast is the summation part, which was concerned with the slope value.

2.2 Method

2.2.1 Stimuli

The stimuli in this study had a circular spatial structure with a 2D Gaussian envelope, which was defined by Equation 2.1. L_0 was background luminance. m was amplitude of cosine function. m was adjusted between 0 and 1 for the positive stimuli that only included positive contrast components and was adjusted between -1 and 0 for the negative stimuli that only included negative contrast components. Higher absolute value of m indicated larger stimulus contrast. m was controlled by a psi method in various trials. f was the spatial structure factor

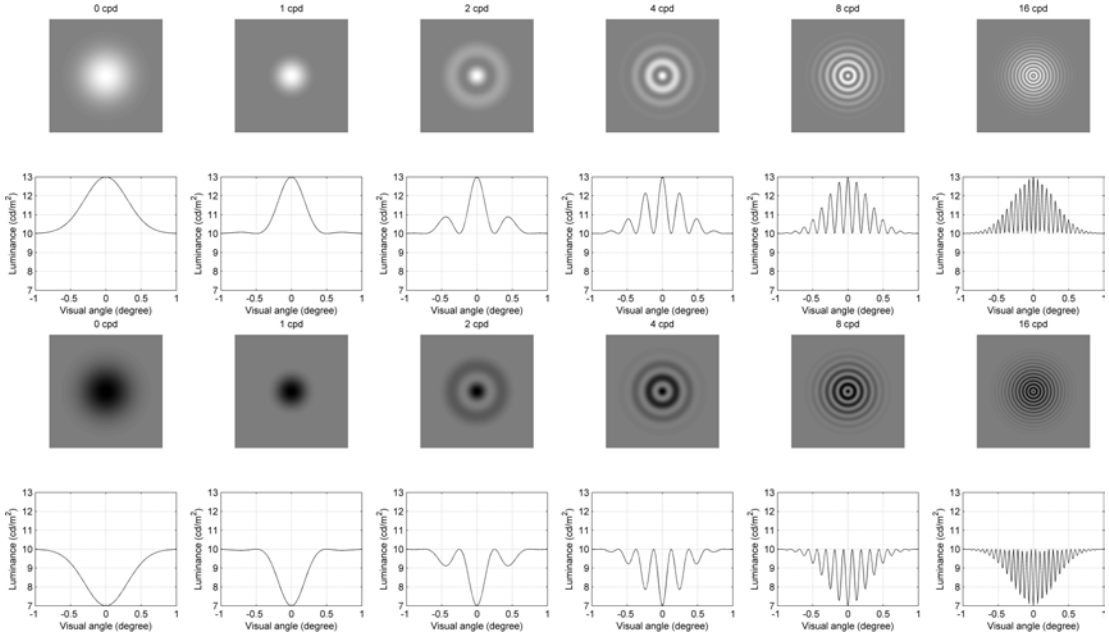

Figure 2.1: Stimulus images and luminance profiles with the same maximum luminance amplitude. The first two rows are for positive contrast stimuli and the last two rows are for negative contrast stimuli. The first and the third rows are images of stimuli in different spatial structures 0, 1, 2, 4, 8, and 16 cpd. The second and the forth rows are luminance profiles of stimuli.

of stimulus. Because Fourier spectrum of stimuli's images includes relatively-large low spatial frequency components, I use the term 'spatial structure' instead of 'spatial frequency' here while cpd is still as the unit to distinguish various spatial structure stimuli. $G(x, y)$ was a 2D normal distribution (Gaussian distribution) function with ± 0.3 degree SD in visual angle. The schema of positive and negative stimulus images and luminance profiles are presented in Figure 2.1.

$$L(x, y) = L_0(1 + m\frac{1 + \cos(2\pi f\sqrt{x^2 + y^2})}{2}G(x, y)) \tag{2.1}$$

2.2.2 Log Contrast Energy Threshold

In a common usage of the double-pulse method, a contrast threshold was measured as the detection threshold. The contrast itself at a certain point, (x, y) could be defined by one-pulse's intensity, $I_T(x, y)$ against background intensity, I_B in a duration of the pulse. In order to compare positive- and negative contrast equitably, contrast, $C(x, y)$ was defined as Equation 2.2 and Equation 2.3. The negative-contrast was transformed into its mirror value along the background intensity axis.

$$C(x, y) = \frac{I_T(x, y)}{I_B}, I_T(x, y) \geq I_B \tag{2.2}$$

$$C(x, y) = \frac{2I_B - I_T(x, y)}{I_B}, I_T(x, y) < I_B \tag{2.3}$$

In order to determine the contrast of the stimuli in different spatial structures, I used the contrast energy concept and defined the contrast energy, C_E as Equation 2.4, which was modified from Watson, Barlow and Robson's definition [Watson et al., 1983].

$$C_E = \frac{1}{mn} \sum_{x=1}^{m} \sum_{y=1}^{n} C^2(x, y) \tag{2.4}$$

$C(x, y)$ was the contrast of the stimulus at (x, y) and counted by each screen pixel. Thus, m and n were the size of the stimulus in pixel. The thresholds for the double-pulse method was defined as the log contrast energy, $log(C_E)$.

2.2.3 Apparatus

Stimuli were presented on a CRT display (CPD G500, SONY) that was controlled by the visual stimulation generator (VSG) system for vision experiments (ViSaGe, Cambridge Research System). The VSG system was configured in 42 bits color mode (14 bits for each phosphor) in 150 Hz frame rate at 640×481 pixel size. The commands to control frame presentation and switch were implemented by the real time sequencer (RTS) of the VSG system through interface functions of the VSG Toolbox for Matlab (Toolbox version 1.27, Matlab version 7.1), which was running on Windows XP operating system.

The CRT display and the chin rest were placed in the dark room which had two chambers separated by a 90mm×65mm window. The distance between the CRT display and the observers' eye was 1800 mm.

2.2.4 Calibration

The luminance and chromaticity coordinates of the CRT monitor were measured by the chromameter (CS-200, Konica-Minolta) and accuracy of the meter and calibration was confirmed by the spectroradiometer (CS-1000, Konica-Minolta). For the calibration of stimuli on the CRT monitor, my own software could directly control the chromameter and firstly stored the data of xy coordinates and luminance in 14336 (2048×7, see Figure 4.5) points on entire gamut area and phosphors' intensity level of the screen. Equal-energy-white in different luminance levels was especially focused (2048 points) for the stimuli in this experiment. The software secondly made the look-up-table with a model to determine RGB digital values for presentation of a certain luminance and chromatic coordinates on

the screen. Before each session, at least 200 random points were measured after one-hour-warming-up of the CRT to confirm the accuracy of the presentation. By this calibration procedure, the error rate of CIE luminance and chromaticity coordinates (x, y, L) on the CRT was less than 3% (see Figure 4.6). The error rate was calculated by

$$error\_rate = \frac{expected\_value - measured\_value}{expected\_value} \times 100$$

Rise and fall time of CRT phosphors, and interval time between two frames were measured with a p-i-n 10 silicon photodiode (Radiometer/Photometer Model 550, EG&G Gamma Scientific Inc.). Peak-to-peak timing error of ISI was less than 3%.

More information about the display model can be seen at corresponding section of Chapter 4.

2.2.5 Procedure

One male and four female students in Kochi University of Technology participated as observers including the author, who was only a non-naive observer. The observers were from 20.5 to 38.0 (the mean, 24.3) years old. All observers had normal color vision tested by Ishihara-plate and D-15, and normal visual acuity ($\pm$1.0 min. of arc. in the visual acuity test with the Landolt C ring).

Two kinds of stimulus configurations, positive- and negative-contrast configurations were tested. Each contrast configuration included stimuli of 6 different spatial structures (0, 1, 2, 4, 8, and 16 cycles per degree). Each spatial structure condition included 14 ISI settings, those were 6.7, 13.3, 20.0, 26.7, 33.3, 40.0,

46.7, 53.3, 60.0, 66.7, 86.7, 106.7, 133.3 and 166.7 msec (in terms of number of frames, 1, 2, 3, 4, 5, 6, 7, 8, 9, 10, 13, 16, 20 and 25 frames (6.7 msec/frame)). These ISI settings were arranged in a pseudo-random order. In each ISI setting, the detection threshold in the log contrast energy was determined by a standard psi procedure [Kontsevich and Tyler, 1999] implemented by Prins and Kingdom [Prins and Kingdom, 2009]. Each setting initially consisted of 20 trials. At the end of the procedure, 10 trials would be appended if the change of estimated threshold at the last 6 trials was beyond pre-set-value or the number of incorrect answer was more than 8. For each observer, detection threshold was measured 5 times as independent sequences in the psi method. In total, about 135,000 trials were performed in this experiment.

At the beginning of each session, the observer adapted to darkness of the experimental room for 5 minutes and to the screen background for another 5 minutes. In each session, there were 4 times of regular breaks, each with 2 minutes. Additionally, the observer could ask for a break after an arbitrary trial when he or she felt tired. A long low-high tone was used to announce the beginning of one trial. The observer pressed any button to begin after he was ready.

The frame sequence of one trial was shown in Figure 2.2. Each trial began with 2 beeps. About 1 sec later, the first pulse (pulse 1) was displayed following ISI frames in presenting only the background, then the second pulse (pulse 2) was displayed. The stimuli were presented in the same quadrant defined by a central fixation cross. The observer was asked to judge the position of the pulses. A beep was played after the observer pressed corresponding button to input the answer.

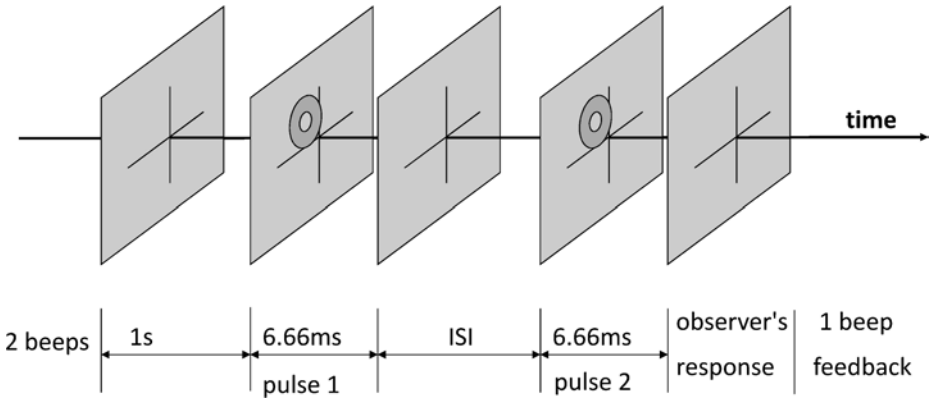

Figure 2.2: Frame sequence of one trial. Gray rectangles indicate frames displayed on the CRT display. From the left to the right, the 1st, 3rd, and 5th frames are background frames and the 2nd and 4th frames are stimulus frames. Two beeps are presented to remind the beginning of the trial and one beep provided a feedback to the observer's response.

2.2.6 Estimation of IRFs

Thresholds were calculated as the average value of the last four turning-points which did not use assumptions about the distribution of threshold values. The psi method was only used to control the contrast of the stimuli. The IRF was estimated from double-pulses thresholds using the working model [Watson, 1986, 1979] with both Watson's model set [Watson, 1986] and Burr's model set [Burr and Morrone, 1993]. Shinomori's estimation method [Shinomori and Werner, 2003] was also used to confirm the estimation results. I presented IRFs only from Burr and Morrone's model set in this chapter while other methods got similar results under the same statistical significant level.

More detail about the estimation of IRFs can be found at Chapter 1. The comparison between the Burr and Morrone's mode set and the Watson's model set is described later.

2.2.7 Statistical analysis

I used two alternative non-parameteric statistics tests, the paired Wilcoxon signed rank test (for paired comparison) and the Wilcoxon rank-sum test (Mann-Whitney's U test) to test the hypotheses because as shown later, the distribution of threshold data is not Normal distribution. Both the paired Wilcoxon signed rank test and the Wilcoxon rank-sum test perform the two-sided test and do not need the Normal distribution assumption.

2.3 Results

2.3.1 Thresholds

Thresholds were estimated as the mean of the last four turning-points which did not use assumptions about the distribution of threshold values. The psi method was only used to control the intensity of stimuli.

Figure 2.3 showed observers' positive- and negative-contrast thresholds (points with error bars in Figure 2.3, each point and error bar were calculated from 5 independent measurements) and model thresholds (continual curves in Figure 2.3, calculated from IRFs using the working model). Positive thresholds were visually higher than negative thresholds in most cases. Statistical tests were used in the following contents to provide more reliable analysis.

2.3.2 Comparison of Thresholds

Figure 2.4 shows the paired comparisons of positive- and negative-contrast thresholds that include 14 ISI settings separately, 6 spatial structure configurations for

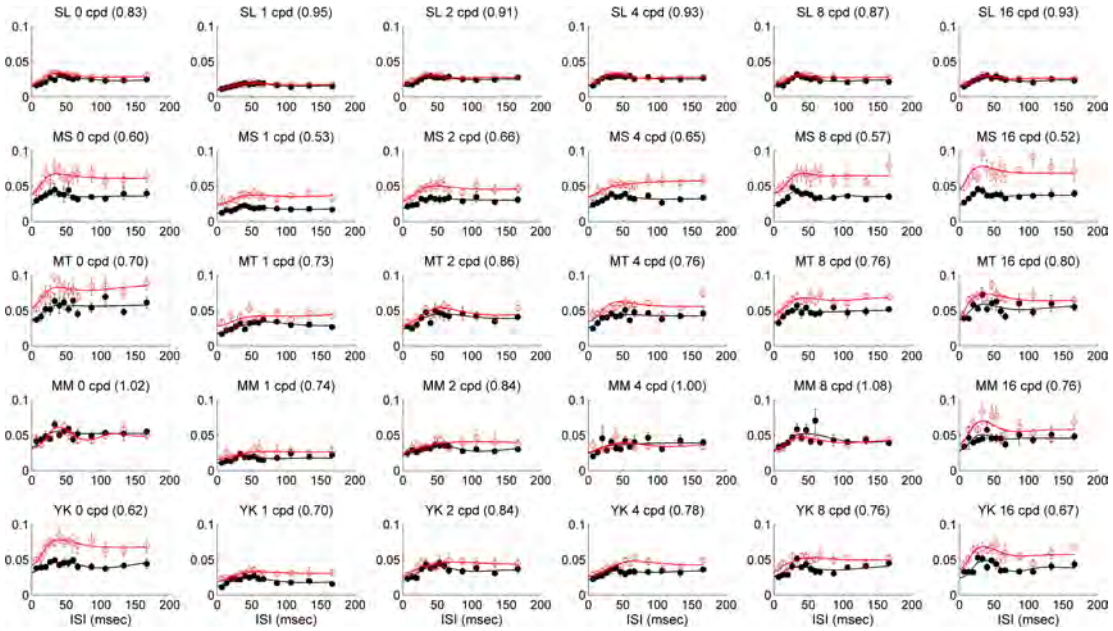

Figure 2.3: Thresholds on all observers. Red curves, empty circles, and lines indicated positive contrast and black curves, filled circles, and lines indicated negative contrast. The first to the fifth rows are for observers SL, MS, MT, MM, and YK, respectively. The first to the sixth columns are for spatial structures 0, 1, 2, 4, 8, and 16 cpd, respectively. Thresholds are the mean of 5 independent measurements (denoted by circles with error bars) and model-thresholds (denoted by smooth curves) calculate from IRFs using the model. Error bars, sometimes smaller than points, indicate ±1 SEM. The abscissa is ISI in millisecond and the ordinate is log contrast energy threshold. The number inside parenthesis at title is the mean-ratio of negative thresholds to positive thresholds.

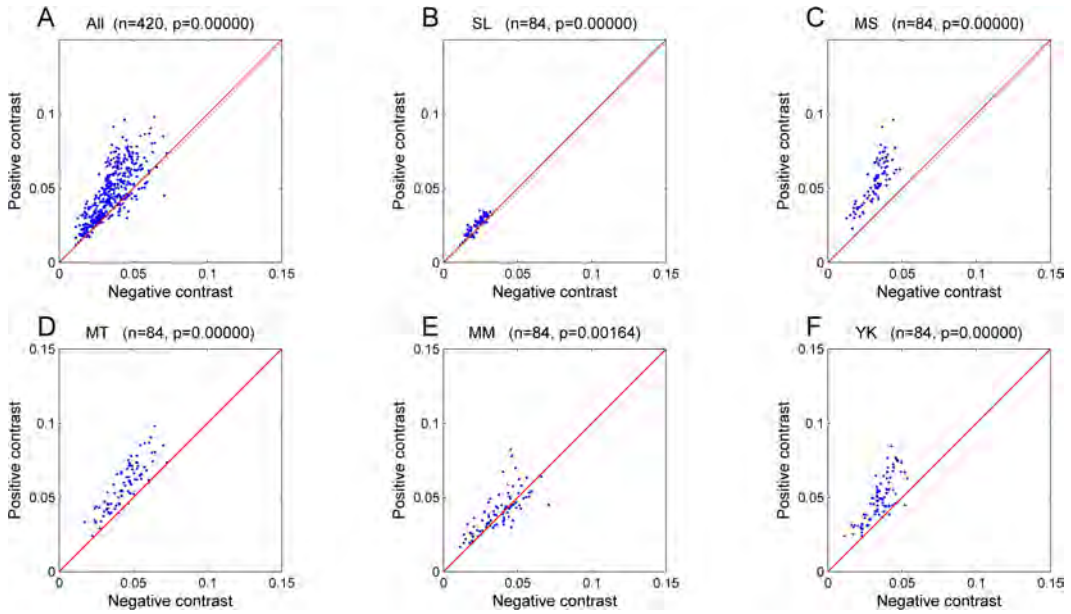

Figure 2.4: Paired comparisons of positive and negative thresholds. The diagonal line denotes equality of positive- and negative-contrast thresholds. Sample size, n and the p-value from the paired Wilcoxon signed rank test are displayed in the title. A: All 5 observers' data together. B-F: Data of observers SL, MS, MT, MM and YK, respectively.

p	0 cpd	1 cpd	2 cpd	4 cpd	8 cpd	16 cpd
SL	0.0000	***0.1100***	0.0064	***0.0705***	0.0004	***0.0718***
MS	0.0000	0.0000	0.0000	0.0000	0.0000	0.0000
MT	0.0000	0.0000	0.0004	0.0000	0.0000	0.0000
MM	***0.5765***	0.0011	***0.3062***	***0.2927***	***0.5346***	0.0000
YK	0.0000	0.0000	0.0084	0.0000	0.0000	0.0000

Table 2.1: The p-value of Wilcoxon rank-sum test to the hypothesis of positive- and negative-contrast thresholds with equal medians. The p-values over 0.05 were indicated by bold and italic fonts.

all 5 observers (420 paired mean-thresholds in total). The diagonal lines denote equality of positive- and negative-contrast thresholds. Most of points are above the diagonal lines and it indicates that positive contrast thresholds are higher than negative contrast thresholds. Paired Wilcoxon signed rank test shows that this difference is statistically significant ($n = 420, p < 0.0000$) for all observers. In Figure 2.4, almost all points locate above the diagonal lines on observers MS (Panel C), MT (D), and YK (F). On observers SL (B) and MM (E), some of points are below the line. The Wilcoxon rank-sum test is used for observers and spatial structure configurations separately and the p-values are listed in Table 2.1. Positive thresholds are significantly different with negative thresholds (at the 0.05 significance level) except observer SL's 1, 4, and 16 cpd, and observer MM's 0, 2, 4, and 8 cpd.

The means of ratios of negative contrast detection thresholds to positive contrast detection thresholds (ς) are listed in Table 2.2. As expected, positive contrast detection thresholds are higher than negative contrast detection thresholds while individual differences exist in part of spatial structures. For example, the values, ς of observer MM's 0, 4, and 8 cpd (denoted by bold and italic fonts) are larger than 1.

ς	0 cpd	1 cpd	2 cpd	4 cpd	8 cpd	16 cpd
SL	0.8336	0.9540	0.9084	0.9348	0.8700	0.9294
MS	0.6106	0.5326	0.6601	0.6538	0.5764	0.5291
MT	0.6970	0.7444	0.8639	0.7596	0.7594	0.8060
MM	***1.0271***	0.7504	0.8595	***1.0194***	***1.0831***	0.7910
YK	0.6246	0.6994	0.8394	0.7907	0.7639	0.6741

Table 2.2: The means of ratios of negative contrast detection thresholds to positive contrast detection thresholds, ς. The ratios, ς, over 1.0 were indicated by bold and italic fonts.

As showed above, positive contrast detection thresholds were significantly higher than negative contrast detection thresholds while individual differences existed in part of spatial structures.

2.3.3 IRFs of Positive- and Negative-Contrast Detection

IRFs of positive- and negative-contrast detection were estimated from various ISI-interval-double-pulse thresholds. The first maximum amplitude of positive IRFs were significant lower than that of negative IRFs. The first and the second peak time of positive and negative IRFs were similar. Figure 2.5 showed similar normalized positive IRFs and negative IRFs.

2.3.4 Paired Comparison of IRFs

IRF shapes in Figure 2.5 qualitatively suggest similarity between positive- and negative-contrast IRFs under the normalization of the peak. Thus, I quantitatively compared six properties of IRFs directly obtained from the shape of each IRF (not from parameters $a_0 \sim a_3$); the peak time of the first (excitatory) phase (1PT+), the peak time of the second (inhibitory) phase (2PT-), the time interval between two peaks (ΔPT), the maximum (positive) amplitude of the first (posi-

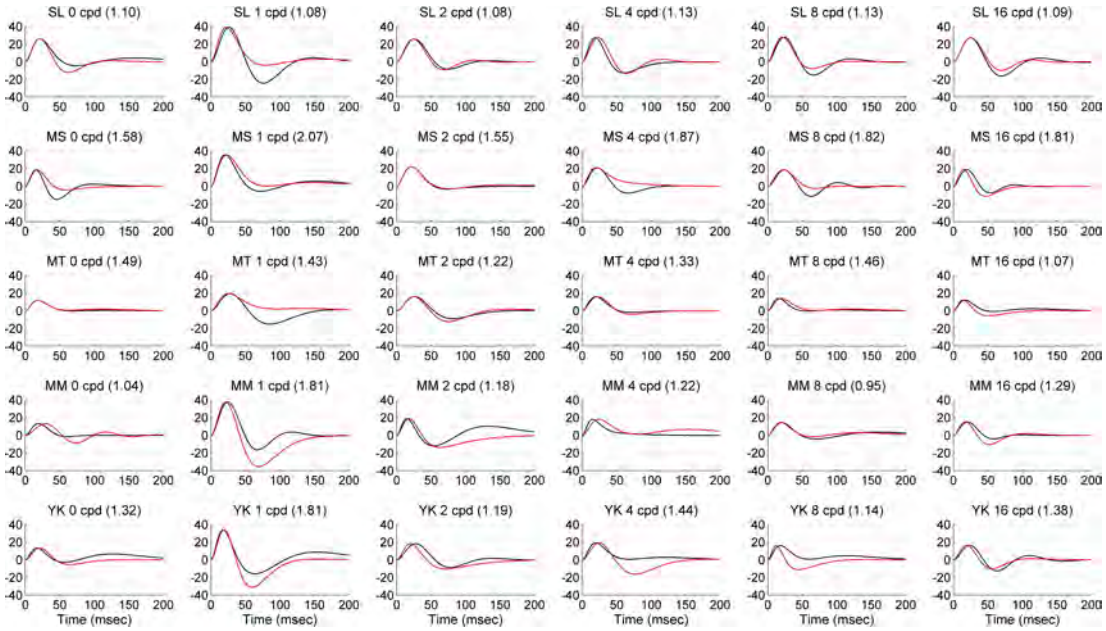

Figure 2.5: IRFs normalized in terms of peak amplitude on all observers. Red curves denote positive contrast IRFs and black curves denote negative contrast IRFs. The first to the fifth rows are for observers SL, MS, MT, MM, and YK, respectively. The first to the sixth columns are for spatial structures 0, 1, 2, 4, 8, and 16 cpd, respectively. All positive IRFs are normalized to match to negative IRFs in each panel, in terms of the peak amplitude. Each normalized factor, which is the enhanced factor for the positive IRF, is shown in the title of the panel. The abscissa is time in millisecond and the ordinate is weighted values of IRFs without dimension (normalized only in positive IRFs as described above).

tive) phase (1MA+), the maximum (negative) amplitude of the second (negative) phase (2MA-), and the ratio of 2PT- to 1PT+ (rPT). Only two lobes were handled because the number of data with more than two lobes was about half in all data including the weak third lobe.

Figure 2.6 shows comparison results of 1PT+, 2PT-, ΔPT, 1MA+, 2MA- and rPT. Two IRFs of observer MS in 4 cpd and observer MM in 4 cpd on both positive- and negative-contrast were excluded in Figures 2.6B, 2.6C, 2.6E and 2.6F, and the corresponding statistic calculation, because of lack of the second phrase. In Figure 2.6 except Panel 2.6D, points were equably distributed around both sides of diagonal lines and the deviations were relatively small. The standard deviation values of 1PT+, 2PT-, ΔPT, 1MA+, 2MA- and rPT are 3.78, 10.03, 7.43, 7.42, 5.97 and 0.32 respectively. In Figure 2.6D (1MA+), most of points are located under the diagonal line. The p-values of paired Wilcoxon signed rank test of 1PT+, 2PT-, ΔPT, 1MA+, 2MA- and rPT are 0.8755, 0.7635, 0.6982, 0.0000, 0.4945, and 0.6570 respectively and the corresponding n values are 30, 28, 28, 30, 28, and 28 respectively. This means that differences between positive- and negative-contrast IRFs are not statistically significant at significance level of 0.05 except 1MA+. After removing data of observer SL's 1, 4, and 16 cpd and observer MM's 0, 2, 4, and 8 cpd data, the p-values of 1PT+, 2PT-, ΔPT, 2MA- and rPT are 0.2228, 0.8892, 0.9223, 0.9095, and 0.3382 respectively (n values are 23, 22, 22, 22, and 22 respectively) and differences between positive- and negative-contrast IRFs are still not statistically significant. The significant difference of 1MA+ is consistent with significant differences between positive- and negative-contrast thresholds.

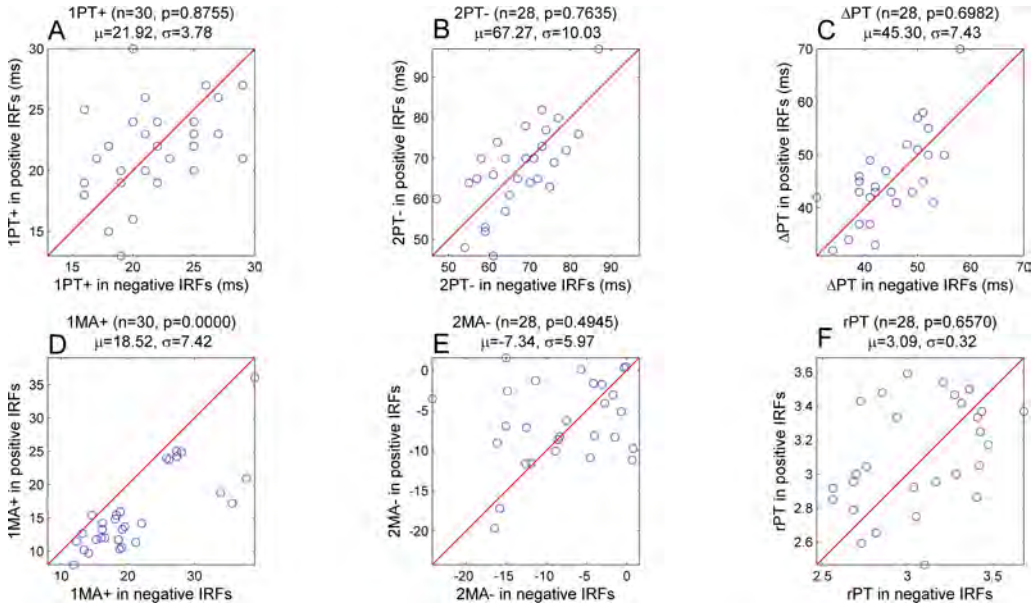

Figure 2.6: Comparisons of six properties between positive- and negative-contrast IRFs. Data come from 5 observers' IRFs on spatial structure 0, 1, 2, 4, 8, and 16 cpd. The sample size n, the p-value of the paired Wilcoxon signed rank test, the mean value, and the standard deviation value are displayed on the title. Diagonal lines denote equal value of positive- and negative-contrast IRFs. A: The peak time of the first (positive) phase (1PT+); B: The peak time of the second (negative) phase (2PT-); C: The time interval between two peaks (ΔPT); D: The maximum (positive) amplitude of the first (positive) phase (1MA+), axis is relative amplitude of IRFs; E: The maximum (negative) amplitude of the second (negative) phase (2MA-); F: The ratio of 2PT- to 1PT+ (rPT).

2.3.5 The Peak Time and the Maximum Amplitude of IRFs

Distributions of these parameters were also estimated using the maximum likelihood estimation method and practically performed by *mle* function in the statistics toolbox of Matlab. Figure 2.7 shows distributions of peak time and maximum amplitude of IRFs from 5 observers' IRFs on 6 spatial structures. The data of 1PT+ could be fitted by the normal distribution with location parameter $\mu = 21.92$, scale parameter $\sigma = 3.75$. The data of 2PT- could be fitted with parameters $\mu = 67.27$ and $\sigma = 9.94$. 1MA+ and 2MA- requires to be fitted by the extreme value distribution with location parameter $\mu = 14.80$, scale parameter $\sigma = 4.79$ and shape parameter $k = 0.18$, and with $\mu = -8.32$, $\sigma = 6.77$ and $k = -0.65$, respectively.

Figure 2.8 shows distributions of 1PT+, 2PT-, 1MA+ and 2MA- for comparison between positive- and negative-contrast IRFs. As the same with Figure 2.7, both positive and negative peak time can be fitted by the normal distribution, and positive and negative maximum amplitude can be fitted by the extreme value distribution. The means and deviations of 1PT+, 2PT-, 1MA+, and 2MA- are reasonably close between the positive- and negative-IRFs. Table 3 shows the confidence intervals of 1PT+, 2PT-, 1MA+, and 2MA- at 98% confidence level. The confidence intervals with estimated distribution-parameters of 1PT+, 2PT- and 2MA- intersect with each other. It indicates similarity between positive- and negative-contrast IRFs. In the case of 1MA+, the confidence interval, μ does not intersect with each other. It indicates that significant difference exists between positive and negative 1MA+ and it is consistent with the statistical analysis de-

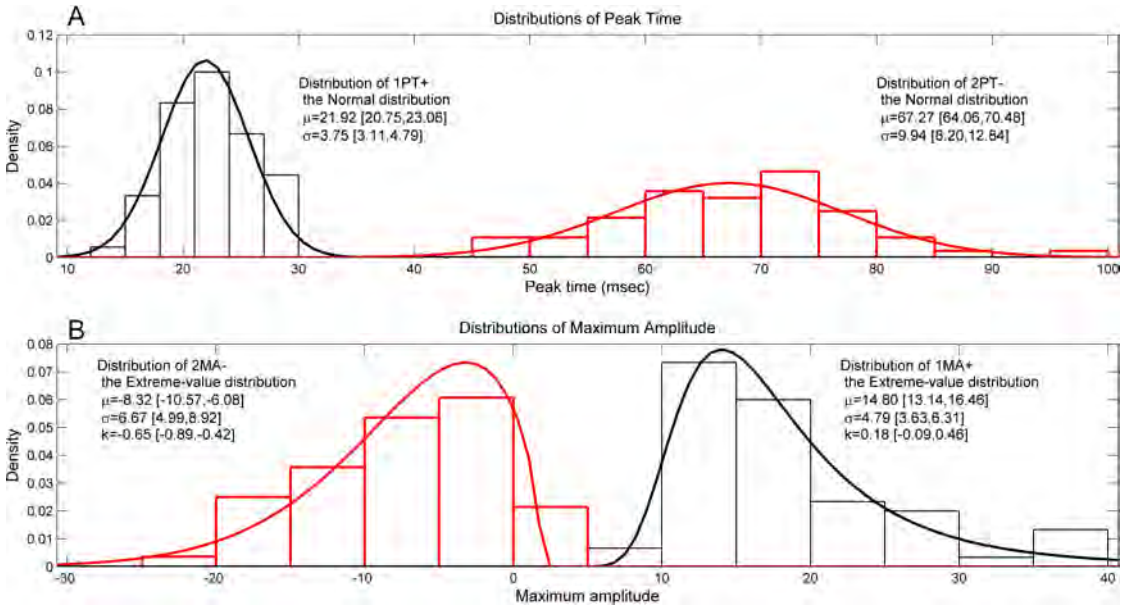

Figure 2.7: Distributions of the peak time and the maximum amplitude. The texts near the probability density function curves were names and parameters (estimated values and confident intervals at 98% confidence level) of the best fitted distributions. A: The histogram and the distribution fit of 1PT+ and 2PT-. B: The histogram and the distribution fit of 1MA+ and 2MA-.

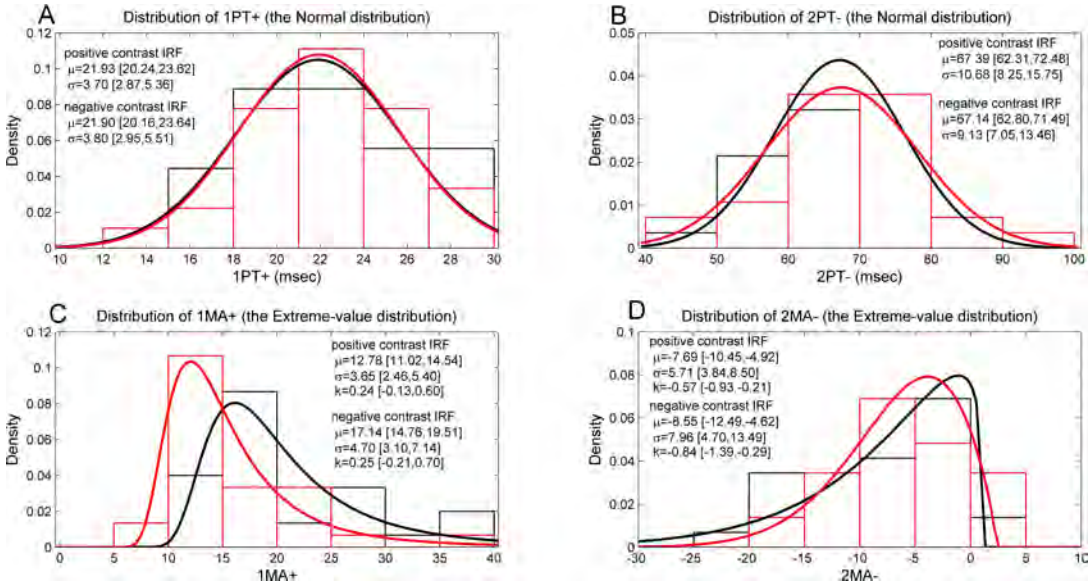

Figure 2.8: Distributions of the peak time and the maximum amplitude for comparing positive- and negative-contrast IRFs. Data come from 5 observers' positive- and negative-contrast IRFs on spatial structure 0, 1, 2, 4, 8, and 16 cpd. Red curves and lines are for positive contrast IRFs and black ones are for negative contrast IRFs. The texts nearby the probability density function curves are parameters (estimated values and confident intervals at 98% confidence level) of the best fit distributions. A: The histogram and the distribution fitting of positive and negative 1PT+. B: The histogram and the distribution fitting of positive and negative 2PT-. C: The histogram and the distribution fitting of positive and negative 1MA+. D: The histogram and the distribution fitting of positive and negative 2MA-.

scribed above. These results indicate that positive- and negative-contrast IRFs are almost identical except the amplitude of the first peak.

ci	1PT+	2PT-	1MA+	2MA-
μ(positive)	[20.24, 23.62]	[62.31, 72.48]	[11.02, 14.54]	[-10.45, -4.92]
μ(negative)	[20.16, 23.64]	[62.60, 71.49]	[14.76, 19.51]	[-12.49, -4.62]
σ(positive)	[2.87, 5.36]	[8.25, 16.75]	[2.46, 5.40]	[3.84, 8.50]
σ(negative)	[2.95, 5.51]	[7.05, 13.46]	[3.10, 7.14]	[4.70, 13.49]

Table 2.3: The confidence intervals of μ and σ in 1PT+, 2PT-, 1MA+, and 2MA- at 98% confidence level. 'Positive' and 'negative' in parenthesis denote the value of positive- and negative-contrast IRFs.

2.3.6 Comparison of calculated IRFs between two model sets

In Watson's model set [Watson, 1986], the IRF was expressed as Equations 2.5, 2.6, and 2.7.

$$h(t) = \xi[h_1(t) - \zeta h_2(t)] \tag{2.5}$$

$$h_1(t) = u(t)[\tau(n_1 - 1)!]^{-1}(t/\tau)^{n_1-1}e^{-t/\tau} \tag{2.6}$$

$$h_2(t) = u(t)[k\tau(n_2 - 1)!]^{-1}(t/(k\tau))^{n_2-1}e^{-t/(k\tau)} \tag{2.7}$$

There were 4 parameters, ξ, ζ, τ, and k (n_1 was set to 3 and n_2 was set to 5 *as the minimum values which can get the best fitting of the data*). Parameters, ξ and ζ were weighting values of two components. Parameter, τ was time constant. Parameter, k was the time constant ratio. $u(t)$ was the unit step function.

The Figure 2.9 shows an example of measured thresholds, IRFs, and the model-thresholds. The green line indicates the Watson model set and the red line indicates the Burr and Morrone model set. Different color and shape points

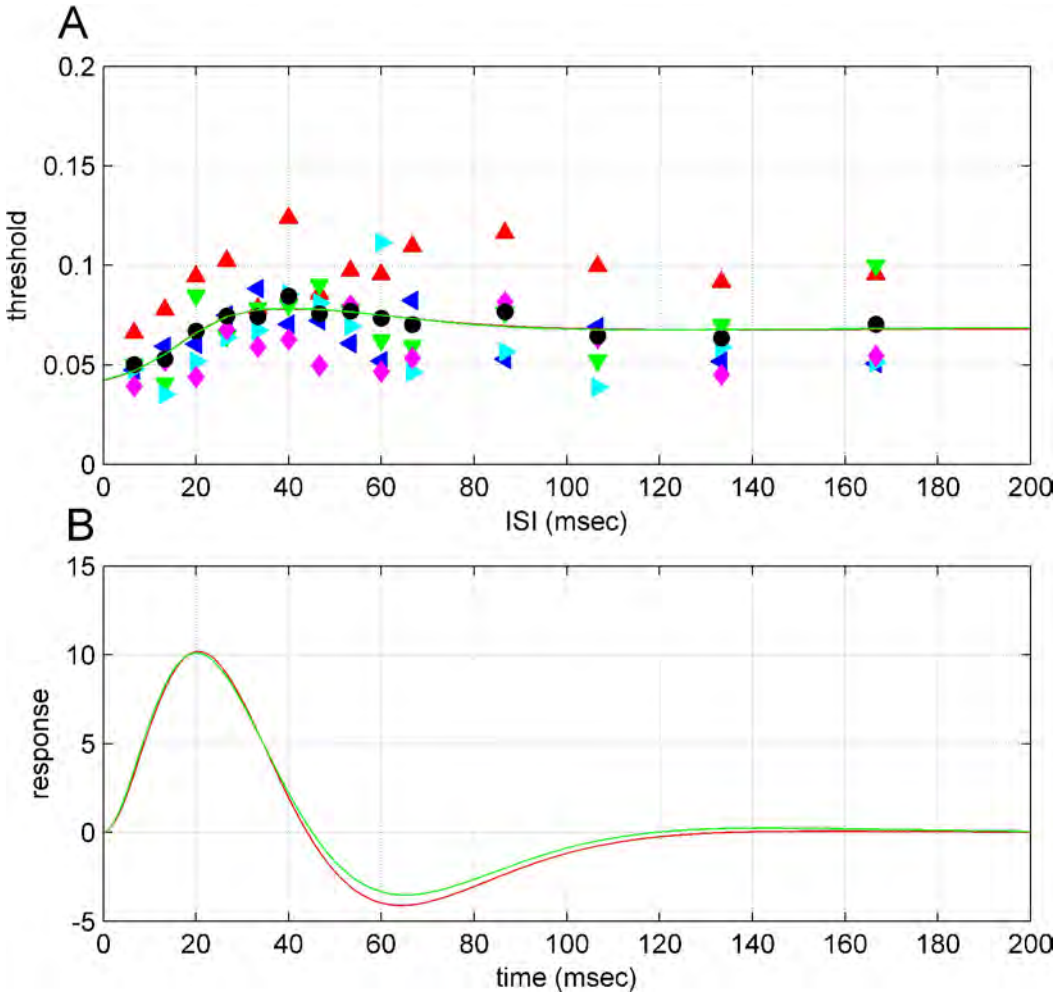

Figure 2.9: Watson model set and Burr and Morrine model set. Data came from observer YK's positive 0 cpd setting. The green line denotes the IRF estimated by the Watson model set and the red line denotes the IRF estimated by the Burr and Morrine model set. A: Measured thresholds (denoted by points in various colors and shapes) and model-thresholds (continual curves). Different color and shape points are used to distinguish thresholds from various sessions except for the filled black circles, which denote the mean values. The abscissa is ISI in milliseconds and the ordinate is the log contrast energy threshold. B: IRFs corresponding to model-thresholds. The abscissa is time in milliseconds and the ordinate is response value without dimension.

Values	Model	1PT+	2PT-	ΔPT	1MA+	2MA-	rPT
μ	B	21.92	67.27	45.30	18.52	-7.34	3.09
	W	22.00	68.45	46.09	18.22	-5.59	3.11
σ	B	3.78	10.03	7.43	7.42	5.97	0.32
	W	3.91	9.09	6.61	7.68	6.27	0.46
p-value	B	0.8755	0.7635	0.6982	0.0000	0.4945	0.6670
	W	0.7355	0.4836	0.2293	0.0000	0.0734	0.4432

Table 2.4: Comparison of parameters, μ, σ and p-values of 1PT+, 2PT-, ΔPT, 1MA+, 2MA-, and rPT between Burr and Morrone model set (B) and Watson model set (W). Means, μ and standard deviations, σ are from both of positive- and negative-contrast IRFs. The p-values are from the paired Wilcoxon signed rank test between the positive contrast IRFs and the negative contrast IRFs.

are used to distinguish thresholds from various sessions except for the filled black circles, which are for the mean values. In most cases, two model sets produced almost identical IRFs. Shinomori's estimation method [Shinomori and Werner, 2003] was additionally used to confirm the estimation results. IRFs estimated by the Burr and Morrone model set are presented in this dissertation.

Table 2.4 shows the similarity between IRFs in the Burr and Morrone model set and Watson model set. Means, μ and standard deviations, σ are from both positive- and negative-contrast IRFs. The p-values are from paired *Wilcoxon signed rank test* between the positive- and negative-contrast IRFs. The μ and σ are close except 2MA- and the statistical significance confirmed by p-values is consistent in both model sets at 1% statistical significance level. The difference in 2MA- is probably caused by different expression of damping in model equations. Table 2.5 shows the confidence intervals of 1PT+, 2PT-, 1MA+, and 2MA- at 98% confidence level by Watson model set. The intervals are basically consistent with those in Table 2.3 by Burr and Morrone model set. However, the confidence intervals of positive and negative μ of 1MA+ intersect under 98% confidence

ci	1PT+	2PT-	1MA+	2MA-
μ(positive)	[19.89, 23.84]	[64.83, 73.92]	***[10.39, 14.40]***	[-7.19, -1.90]
μ(negative)	[20.59, 23.68]	[63.58, 71.59]	***[14.07, 19.32]***	[-10.51, -3.57]
σ(positive)	[3.36, 6.26]	[7.91, 13.91]	[2.67, 6.00]	[3.37, 8.87]
σ(negative)	[2.63, 4.91]	[6.66, 12.57]	[3.35, 7.78]	[4.66, 11.87]

Table 2.5: The confidence intervals of μ and σ in 1PT+, 2PT-, 1MA+, and 2MA- at 98% confidence level. Positive and negative in parentheses denote the confidence intervals of positive- and negative-contrast IRFs. The intersected intervals of μ in 1MA+ are denoted by bold and italic fonts.

level in IRFs by Watson model set, although they do not intersect under 95% confidence level.

Table 2.6 shows normalization factor value that is the ratio to match the first peak amplitude of the positive-contrast IRF to the one of the negative-contrast IRF. The values of this factor in Burr and Morrine model are the same as those shown in Figure 2.5. With this factor value, however, the difference between Burr and Morrone model set and Watson model set is large. In 9 of 30 conditions for observers and spatial structures, the difference is more than 10%.

2.4 Discussion

As described in Introduction, in this study, I tried to compare the detection thresholds of double pulses between positive- and negative-contrast stimuli and to investigate the temporal characteristics of positive- and negative-contrast detection through IRFs. Results indicated that positive contrast detection thresholds were significantly higher than negative contrast detection thresholds. However, there was no significant difference at three conditions on one observer and four conditions on another one observer. Moreover, the IRFs of positive contrast were

Observer	Model	0 cpd	1 cpd	2 cpd	4 cpd	8 cpd	16 cpd
SL	B	1.10	1.08	1.08	1.13	1.13	1.09
	W	1.11	1.03	1.10	1.18	***1.34***	1.12
MS	B	1.58	2.07	1.55	1.87	1.82	1.81
	W	***1.38***	2.08	1.59	***1.65***	***2.45***	***2.02***
MT	B	1.49	1.43	1.22	1.33	1.46	1.07
	W	1.48	1.47	1.22	1.39	1.44	1.04
MM	B	1.04	1.81	1.18	1.22	0.95	1.29
	W	***0.93***	1.85	1.29	1.20	0.97	***1.17***
YK	B	1.32	1.81	1.19	1.44	1.14	1.38
	W	1.23	1.65	***1.04***	1.42	1.11	***1.60***

Table 2.6: Comparison of normalization factor of IRFs between Burr and Morrone model set (B) and Watson model set (W). The normalization factor is the ratio to match the first peak amplitude of the positive-contrast IRF to the one of the negative-contrast IRF. The values in Burr and Morrine model are the same as those shown in Figure 3B. The data sets are denoted by bold and italic font if the difference is more than 10%.

similar with the IRFs of negative contrast. I discussed about these results and additionally the possible source of different sensitivity according to the working model.

2.4.1 Difference of double-pulse thresholds between positive- and negative-contrast

As described in the Introduction, previous literature reported conflicting results regarding positive- and negative-thresholds. The results on 4,200 threshold-samples from about 135,000 trials indicated that positive contrast detection thresholds were higher than negative contrast detection thresholds, with the exception of observer SL's 1, 4, and 16 cpd and observer MM's 0, 2, 4, and 8 cpd. I considered four possible reasons for this conflict.

Individual differences in detection threshold on various spatial structures could

be the *first* reason why different investigators reported conflicting results in various conditions. In this research, negative-contrast thresholds are larger for only one observer (MM) in some spatial structure (0, 4 and 8 cpd). Even for this observer, however, negative contrast thresholds are smaller in other conditions (1 and 16 cpd) with statistical significance. Although I do not have a rational model to explain this change depending on spatial structure and why it occurred only for this observer, this kind of individual difference can cause the conflicting results between researches.

The comparison between positive- and negative-contrast thresholds was taken under comparable conditions, not only stimuli condition but also contrast definition condition. The only difference between positive- and negative-condition was the contrast polarity controlled by the parameter, m in Equation 2.1. This difference was dispelled by the definition of negative contrast thresholds defined as its mirror value along the background intensity axis (see Equation 2.3). Thus, the difference between thresholds was not caused by the asymmetrical log function that I used in the definition of the log contrast energy.

In terms of the model analysis, I considered the working model, the differences between positive and negative thresholds might be caused by the linear filter part, the summation part, or both. The results show that positive and negative IRFs are similar, which supported the notion that the temporal characters of the linear filter are basically the same between positive- and negative-contrast detection. Thus, there is a high possibility that threshold differences originate from the summation part. I compared the slope values (β, estimated using the psychometric function described at Chapter 4) between positive- and negative-contrast detections using the Wilcoxon rank-sum test with separated observers'

data. The result of this analysis indicated that positive contrast slope values were not significantly different with negative contrast slope values for observer MM ($n = 84, p = 0.2930$). On the contrary, for observers SL ($n = 84, p = 0.0422$), MS ($n = 84, p < 0.0001$), MT ($n = 84, p = 0.0274$), and YK ($n = 84, p < 0.0001$), positive contrast slope values were significantly different from negative contrast slope values under the 0.05 significant level. This result is consistent with the threshold result that positive- and negative-contrast thresholds of observer MM's 0, 2, 4, and 8 cpd are not significantly different. It is worth to notice that observer SL's p-value is close to 0.05 while the positive- and negative-contrast contrast thresholds are not significantly different at observer SL's 1, 4, and 16 cpd. It supports the notion that significant differences of thresholds originate from differences of slope values in Minkowski summation instead of IRFs of linear filters.

The result is supported by physiological and anatomical researches. Physiological and anatomical differences of ON- and OFF-cells can have important role in positive and negative thresholds. Watson thought that the difference of thresholds is generally caused by the difference of ON- and OFF-center cells [Watson, 1986]. Moreover, this difference of thresholds might be caused by the different structures (size and cone type) of receptive fields of ON- and OFF-cells. Chichilnisky and Kalma reported that the receptive fields of ON cells were larger in diameter than those of OFF cells [Chichilnisky and Kalmar, 2002]. They also mentioned that if cells with smaller receptive fields are more closely spaced, a larger number of OFF cells than ON cells may encode a given stimulus. Field et al. reported that the ON- and OFF- midget and parasol cells each sampled the complete population of L- and M-cones [Field et al., 2010]. By combining those

two results, I can expect that the number of OFF cells is higher than that of ON cells in the same area. Those results supported the notion/theory that negative contrast thresholds were lower than positive contrast thresholds.

2.4.2 Similarity in impulse responses

The similarity between positive- and negative-contrast IRFs indicates that the temporal characteristics of the initial stage of visual system for positive- and negative-contrast detections are similar. However, I have to mention the accuracy of the data. The time duration of a single frame displayed on the CRT was 6.7 msec in the experiment. Considering the 3% peak-to-peak timing error, the temporal resolution in the experiment was about 7 msec. Thus, the possibility that less than 7 msec temporal differences of IRFs may still exist was not indicated by the data.

This similarity is reasonable because the complete population of L- and M-cones was sampled by the ON- and OFF- midget and parasol cells [Field et al., 2010] and the same population should not cause differences in temporal characteristics. Evidence from physiological research showed that ON- and OFF-responses of retinal cells were similar in experiments with cats [Kruger and Fischer, 1975] and macaques [Kremers et al., 1993] and black-responses dominated macaque V1 [Yeh et al., 2009]. This evidence supports my finding that differences of ON- and OFF-responses were located after retina, if they exist, rather than at retina. In vitro electrode recordings from the retinal ganglion cells of macaques showed that L-OFF cells had slower response than L-ON cells (about 13%, 5 msec, longer at the peak) under a 15 or 8.33 msec stimulus display interval, which is the temporal

resolution of the experiment [Chichilnisky and Kalmar, 2002]. However, many others reported similar characteristics between ON- and OFF-cells [Benardete and Kaplan, 1999, 1997; Kremers et al., 1993; Pandarinath et al., 2010]. These results were consistent with my results.

Before the experiment, it was expected that the difference of spatial frequency component of stimuli would cause some differences of IRFs in temporal characteristics because of the difference of receptive field size between ON- and OFF-cells [Chichilnisky and Kalmar, 2002]. However, the difference was not observed in the data. In this study, all spatial structure stimuli (0,1,2,4,8, and 16 cpd) included relatively strong low spatial frequency component in their Fourier spectrums because I focused about comparison between positive- and negative contrasts and the low spatial frequency component corresponds this parity of contrasts. Thus, there is the possibility that the stimuli used in this study were dominated by the low spatial-frequency-tuned channel and were not so much sensitive to higher spatial-frequency-tuned channels.

2.4.3 Peak time of IRFs

The means of the first (excitatory) peak time (1PT+) and the secondary (inhibitory) peak time (2PT-) are 22.0 msec ($\sigma = 3.78$) and 67.0 msec ($\sigma = 9.97$), respectively. This is consistent with Shinomori and Werner's results [Shinomori and Werner, 2003]. The mean of the peak difference (ΔPT) is 45.0 msec ($\sigma = 7.39$). The mean of ratio 2PT-/1PT+ is 3.09 ($\sigma = 0.31$).

As mentioned previously, the distributions of peak time of IRFs can be explained by the normal distribution and the distributions of amplitude of IRFs

can be explained by the extreme-value distribution. The normal distribution was symmetric and the extreme-value distribution was asymmetric. Different distributions reflected different variation regularity of the peak time and the maximum amplitude.

2.5 Conclusion

It is concluded that positive- and negative-contrast impulse responses were similar while the sensitivity of positive- and negative-contrast detection was different. This sensitivity difference originates from the summation part rather than the linear filter part of the visual system.

Chapter 3

IRFs of Spatial-Frequency-Tuned-Channels

In this chapter, double-pulse thresholds of contrast detection using stimuli with ring-structure Fourier spectrum at different spatial frequencies were measured psychophysically on human observers in order to get IRFs and then to investigate the impulse responses and the sensitivities of the possible spatial-frequency-tuned channels.

Results showed that: (1) the double-pulse detection thresholds of lower spatial frequencies (1 and 2 cycle per degree (cpd)) were lower than those of higher spatial frequencies (8 and 16 cpd), and (2) IRFs of lower spatial frequencies (1 and 2 cpd) were significantly different with IRFs of higher spatial frequencies (8 and 16 cpd) both on the phase, the first zero-crossing time, and the amplitude. The lower spatial frequencies had two or three phases while the higher spatial frequencies had only one phase (except one observer had very weak second phase). The first zero-crossing time of IRFs of lower spatial frequencies were shorter and the

amplitude of IRFs of lower spatial frequencies were higher, compared to those of higher spatial frequencies. (3) The peak frequency of temporal contrast sensitivity function (tCSF) derived from IRFs was higher in lower spatial frequencies (1 and 2 cpd) than that in higher spatial frequencies (8 and 16 cpd). The results indicated that at least two kinds of spatial-frequency-tuned channels, the lower- and higher-spatial-frequency-tuned channels that dominates the detection of lower spatial frequencies (1 and 2 cpd) and the detection of high spatial frequencies (8 and 16 cpd), respectively, exists in human vision. However, the accurate number of spatial-frequency-tuned channels could not be estimated because of the possible limit of measurement with the double pulse method for the IRF that is using the detection threshold.

3.1 Introduction

The spatial frequency was defined as an oscillation of luminance or color in space by De Valois [De Valois and De Valois, 1990]. The spatial frequency is usually measured by the repeat of sinusoidal components which is determined by the Fourier transform.

The exploration of spatial-frequency-tuned channels was pioneered by Campbell and Robson whose results supported that independent mechanisms sensitive to limited ranges of spatial frequencies existed [Campbell and Robson, 1968] and was followed by the research about an selective adaptation effect for spatial frequency [Blakemore and Campbell, 1969]. Evidences have been provided that human vision contains different narrow ranges of spatial-frequency-tuned channels through comparing detection of simple sinusoidal gratings and complex gratings

which sum two sinusoids with various frequencies [Graham and Nachmias, 1971; Sachs et al., 1971]. In previous literature, these spatial-frequency-tuned channels have been considered as spatial channels, which are not incidentally spatial-frequency-tuned but must be inevitably tuned in narrow band for the purpose of spatial information processing. The number of spatial-frequency-tuned channels has been considered as 4 [Wilson and Bergen, 1979], 6 [Wilson et al., 1983] and 7 [Anderson and Burr, 1985]. Recent spatial contrast detection model [Watson and Ahumada, 2005] included contrast sensitivity filter, oblique effect filter, and parallel spatial frequency and orientation channels, followed by the Minkowski summation and the model has 11 spatial channels. Many investigations about spatial channels concentrated on the spatial contrast sensitivity function (CSF), which described the relationship between contrast sensitivity and spatial frequency. The CSF was thought as the envelop of spatial frequency tuning curve of a number of narrow and independent visual channels [Campbell and Robson, 1968; Sachs et al., 1971; Wilson et al., 1983].

Wilson and Wilkinson thought, however, that the assumptions of multiple spatial channels have been broken on channel linearity, parallelism, and independency except detection threshold [Wilson and Wilkinson, 2004]. There is the opinion [Logvinenko, 2003] that the fundamental questions of spatial channels remain controversial because localized adaptation effect at a certain spatial frequency [Blakemore and Campbell, 1969; Campbell and Robson, 1968], for example, cannot be the evidence of multiple channels but it may reflect the multiple analyzer within a single channel. Although it is much true in the viewpoint of mathematical model, some physiological evidences (See [Nishimoto et al., 2005, 2006]) support that multiple spatial channels originated from signals from differ-

ent receptive fields in size at retina. Thus, the standing point in this study is that, at least, the multiple spatial-frequency-tuned channels can exist and they possibly have different temporal characteristics, but it could be difficult to confirm the number of channels from psychological data.

IRFs of various spatial frequencies were measured in order to investigate the temporal characteristics of possible spatial-frequency-tuned channels. The IRF can be estimated from double-pulse detection thresholds. Detection threshold as a criterion in this study provides a safety assurance of linearity. Without assumption about channel independency, the temporal characteristics of spatial-frequency-tuned channels, which were stimulated by spatial frequency stimuli with separately circular structure Fourier spectrum, were investigated by IRFs.

3.2 Method

3.2.1 Stimuli

The stimuli were defined by the Equation 3.1. $L(x, y)$ was the luminance of stimuli. The factor f indicated the spatial frequency. $G(x, y)$ was the 2-D Gaussian distribution function. The operator fft indicated the 2-D fast Fourier transform and the operator fft^{-1} indicated the reversed 2-D fast Fourier transform. The operator flt indicated the operation that set the Fourier spectrum components as zero except the circular part corresponded with the spatial frequency f. The contrast intensity of the stimuli was controlled by the factor $m(m > 0)$ which could adjust the contrast of the stimuli without changing neither the mean luminance of the stimuli nor the relational structure of its Fourier spectrum components.

L_0 was the background luminance which equalled with the average luminance of the stimulus (10 cd/m^2).

$$L(x,y) = L_0(1 + mfft^{-1}(flt(fft(\cos(2\pi f\sqrt{x^2+y^2})G(x,y))))) \tag{3.1}$$

The stimulus with a circular structure Fourier spectrum showed in Figure 3.1. The stimuli images had circular 2D-Fourier spectrum components at spatial frequencies 1, 2, 4, 8, and 16 circles per degree (cpd). The average luminance of stimuli, equalling the background luminance, was 10 cd/m^2. The chromatic coordinates of the stimulus and the background were set to the equal-energy-white, $(0.3333, 0.3333)$ in chromatic coordinate of CIE 1931.

Stimuli were presented in one of four quadrants defined by a central fixation cross and a rectangle border at a 10 cd/m^2 background which had the same chromaticity with the stimulus (equal-energy-white). Both of height and width of the center cross were 2 degree in visual angle. The four positions of the stimuli were located 0.71 degree to one side or the other and 0.71 degree above or below to the center of the fixation cross. The background size was about 4 degree height and 6 degree width.

3.2.2 Log Contrast Threshold

In a common usage of the double-pulse method, a contrast threshold was measured as the detection threshold. The contrast C was defined by the peak amplitude of one-pulse's intensity I_T against background intensity I_B in a duration of the pulse when the pulse intensity was the same. The thresholds for the double-

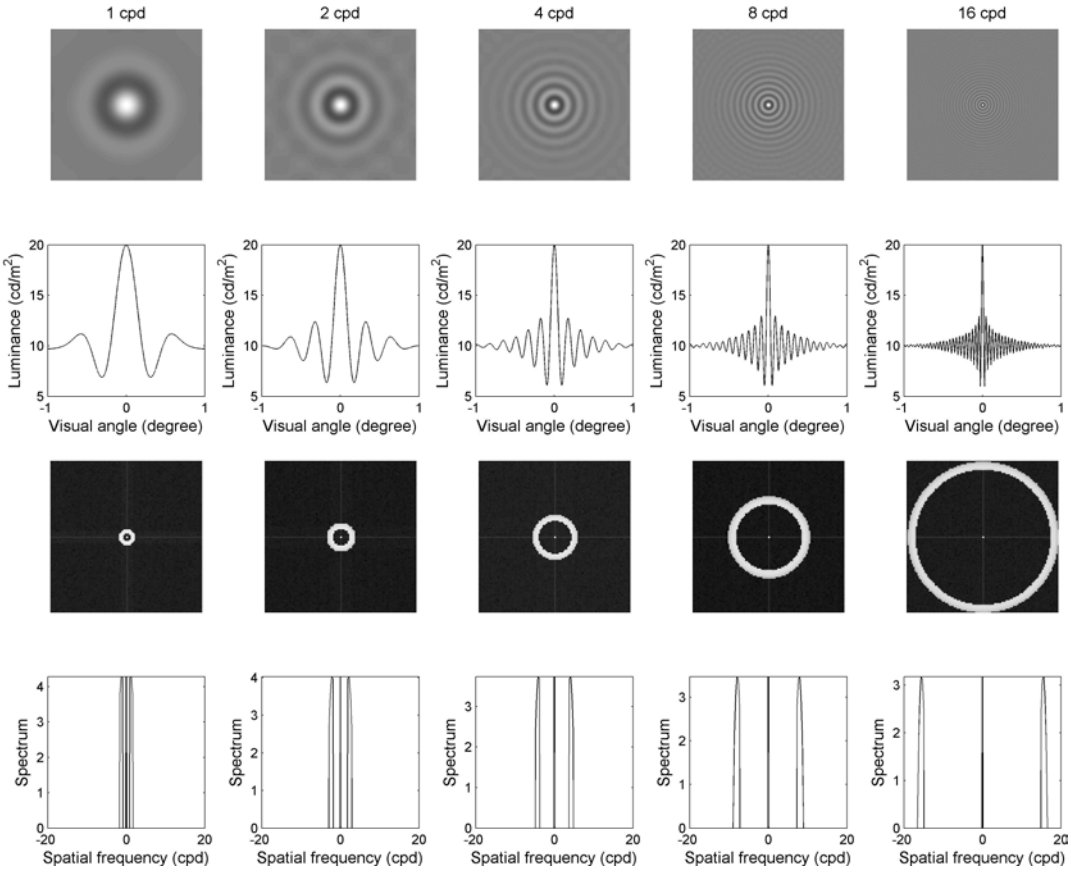

Figure 3.1: Stimuli images, stimuli profiles, Fourier spectrum, and spectrum profiles. Five columns indicate spatial frequencies 1, 2, 4, 8, and 16 cpd. The first row includes the images of stimuli in various spatial frequencies. The second row includes the luminance profiles of stimuli. The third row includes images of the Fourier spectrum (in log scale) of the stimuli images. The fourth row includes the profiles of the Fourier spectrum (in log scale).

pulse method was defined as the log contrast, $log(C)$. The log contrast energy and the Fourier-spectrum contrast were also used for comparison.

3.2.3 Apparatus

Stimuli were presented on a CRT display (CPD G500, SONY) that was controlled by the visual stimulation graphic (VSG) system for vision experiments (ViSaGe, Cambridge Research System). The VSG system was configured in 42 bits color mode (14 bits for each phosphor) in 150 Hz frame rate at 640×481 pixel size. The commands to control frame presentation and switch were implemented by the real time sequencer (RTS) of the VSG system through interface functions of the VSG Toolbox for Matlab (Toolbox version 1.27, Matlab version 7.1), which was running on Windows XP operating system.

The CRT display and the chin rest were placed in the dark room which had two chambers separated by a 90mm×65mm window. The distance between the CRT display and the observers' eye was 1800 mm.

3.2.4 Calibration

The luminance and chromaticity coordinates of the CRT monitor were measured by the chromameter (CS-200, Konica-Minolta) and accuracy of the meter and calibration was confirmed by the spectroradiometer (CS-1000, Konica-Minolta). For the calibration of stimuli on the CRT monitor, my own software could directly control the chromameter and firstly stored the data of xy coordinates and luminance in 14336 (2048×7, see Figure 4.5) points on entire gamut area and phosphors' intensity level of the screen. Equal-energy-white in different luminance

levels was especially focused (2048 points) for the stimuli in this experiment. The software secondly made the look-up-table with a model to determine RGB digital values for presentation of a certain luminance and chromatic coordinates on the screen. Before each session, at least 200 random points were measured after one-hour-warming-up of the CRT to confirm the accuracy of the presentation. By this calibration procedure, the error rate of CIE luminance and chromaticity coordinates (x, y, L) on the CRT was less than 3% (see Figure 4.6). The error rate was calculated by

$$error\_rate = \frac{expected\_value - measured\_value}{expected\_value} \times 100$$

Rise and fall time of CRT phosphors, and interval time between two frames were measured with a p-i-n 10 silicon photodiode (Radiometer/Photometer Model 550, EG&G Gamma Scientific Inc.). Peak-to-peak timing error of ISI was less than 3%.

3.2.5 Procedure

One male and four female students in Kochi University of Technology were participated as observers including the author, who was only a non-naive observer. The observers were aged from 21.5 to 39 (the mean was 25.3). All observers had normal color vision tested by Ishihara-plate and D-15 and normal visual acuity ($\pm$1.0 min. of arc. in the visual acuity test with the Landolt ring).

Five stimuli with spatial frequencies 1, 2, 4, 8, and 16 cpd were included in experiment. Each spatial frequency condition included 14 ISI settings (13.4, 26.8, 33.5, 40.2, 46.9, 60.3, 73.7, 87.1, 100.5, 120.6, 140.7, 160.8, 187.6, and 201.0

msec; in terms of number of frames, 2, 4, 5, 6, 7, 9, 11, 13, 15, 18, 21, 24, 28, and 30 frames, 6.7 msec/frame). These ISI settings were arranged in a pseudo-random order. In each ISI setting, the detection threshold in the log contrast energy was determined by a standard psi procedure [Kontsevich and Tyler, 1999] implemented by Prins and Kingdom [Prins and Kingdom, 2009]. Each setting initially consisted of 20 trials. At the end of the procedure, 10 trials would be appended if the change of estimated threshold at the last 4 trials was beyond pre-setting-value or the number of incorrect answer was more than 10. For each observer, detection threshold was measured 5 times as independent sequences in the psi method. In total, about 40,000 trials were included in this experiment.

At the beginning of each session, the observer adapted to darkness of the experimental room for 5 minutes and to the screen background for another 5 minutes. In each session, there were 4 times of regular breaks, each with 2 minutes. Additionally, the observer could ask for a break after an arbitrary trial when he felt tired. A long low-high tone was used to announce the beginning of an ISI setting. The observer pressed a button to begin after he was ready.

Frame sequence of one trial was similar with Figure 2.2. Each trial began with 2 beeps. About 200 milliseconds later, the first pulse was displayed following ISI frames in presenting only the background, and then the second pulse was displayed. The stimuli were presented in one of the four quadrants defined by a central fixation cross. The observer was asked to judge the position as to where the stimulus was displayed. A feedback beep was played after the observer pressed corresponding button to input the answer.

3.2.6 Estimation of IRFs

Thresholds were calculated as the average value of the last four turning-points which did not use assumptions about the distribution of threshold values. The psi method was only used to control the contrast of the stimuli. The IRF was estimated from double-pulses thresholds using the working model [Watson, 1986, 1979] with both Watson's model set [Watson, 1986] and Burr's model set [Burr and Morrone, 1993]. Shinomori's estimation method [Shinomori and Werner, 2003] was also used to confirm the estimation results. We presented IRFs only from Burr and Morrone's model set in this chapter while other methods got similar results under the same statistical significant level.

More detail about the estimation of IRFs can be found at Chapter 1.

3.3 Results

The temporal impulse response functions (IRFs) were measured in order to investigate temporal characteristics of possible spatial-frequency-tuned channels (SFTC) of human vision. Stimuli with ring-structure Fourier spectrum at spatial frequencies 1, 2, 4, 8, and 16 cpd were used in the measurement of double-pulse contrast detection thresholds on five observers. IRFs were estimated from sequential double-pulse contrast detection thresholds.

Results showed that: (1) the double-pulse detection thresholds of lower spatial frequencies (1 and 2 cpd) were lower than those of higher spatial frequencies (8 and 16 cpd), and (2) IRFs of lower spatial frequencies (1 and 2 cpd) were significantly different with IRFs of higher spatial frequencies (8 and 16 cpd) both in the phase, the first zero-crossing time, and the amplitude. The lower spatial frequencies

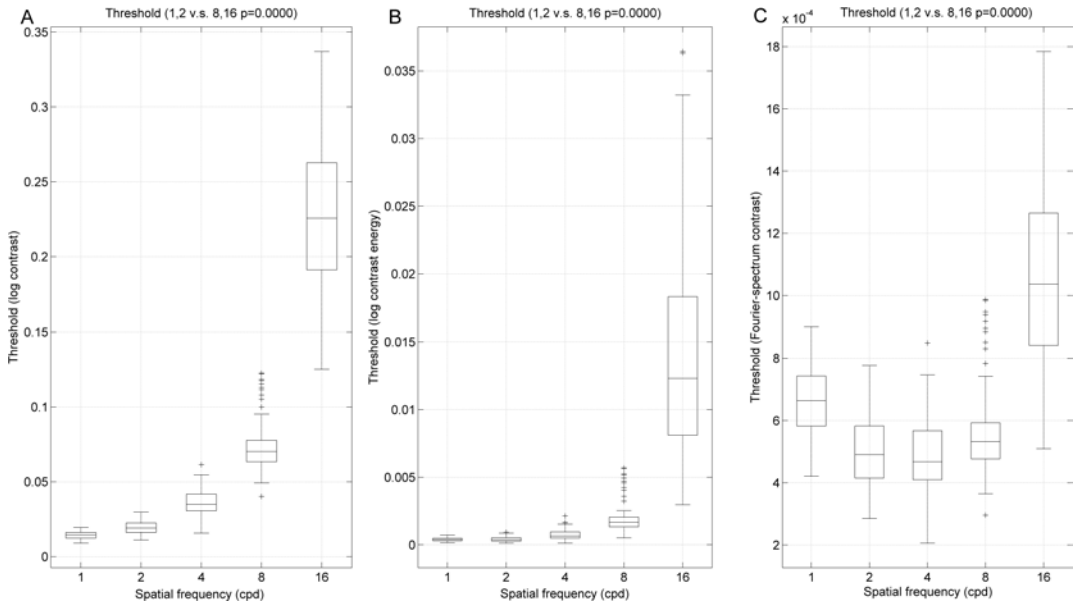

Figure 3.2: Box plots of the log contrast (panel A), the log contrast energy threshold (panel B), and the Fourier-spectrum contrast threshold (panel C). The abscissa is the spatial frequency in cpd and the ordinate are the log contrast (panel A), the log contrast energy (panel B), and the Fourier-spectrum contrast (panel C). The p-value of the Wilcoxon rank-sum test between thresholds of the lower spatial frequencies (1 and 2 cpd) and the higher spatial frequencies (8 and 16 cpd) is displayed on the title of panels. The threshold values of panel C were gotten using the following equation $C_F = k_f\sqrt{C_E}$. C_E is the log contrast energy, C_F the Fourier-spectrum contrast, k_f factor of spatial frequency f. The values of k_f are 0.03369 (1 cpd), 0.02541 (2 cpd), 0.01838 (4 cpd), 0.01308 (8 cpd), and 0.00935 (16 cpd) respectively. 'p=0.0000' donates the p-value is less than 0.0001.

had two or three phases while the higher spatial frequencies had only one phase (except one observer had very weak second phase). The first zero-crossing time of IRFs of lower spatial frequencies were shorter and the amplitude of IRFs of lower spatial frequencies were higher, compared to those of higher spatial frequencies. (3) The peak frequency of temporal contrast sensitivity function (tCSF) derived from IRFs was higher in lower spatial frequencies (1 and 2 cpd) than that in higher spatial frequencies (8 and 16 cpd).

Spatial frequency	1 cpd	2cpd	4 cpd	8 cpd	16 cpd
Observer SL	3	3	3	1	2
Observer MS	2	3	1	1	1
Observer MT	3	3	1	1	1
Observer MM	3	2	3	1	1
Observer YK	2	3	2	1	1

Table 3.1: Phase count of IRFs. Numbers in table cells indicate corresponding phase count of IRFs.

3.3.1 Threshold

Figure3.2 showed the box plot of the threshold. The threshold values were displayed in Figure3.3. The differences between the lower spatial frequency and the higher spatial frequency was statistically significant ($p < 0.0001$) on both the log contrast threshold, the log contrast energy threshold, and the Fourier-spectrum contrast threshold defined in Chapter 4.

3.3.2 IRF

Figure 3.3 showed all five observers' thresholds, model thresholds, and IRFs at spatial frequencies 1, 2, 4, 8, and 16 cpd. A very small part of thresholds in part of session at part of ISI setting were identified as the outlier and were skipped when calculated the mean threshold. Visually, the phase of IRFs at lower spatial frequencies were different with those at higher spatial frequencies. More details were showed in the following contents.

3.3.2.1 Phase of IRFs

The phase of IRF was calculated by following rules. The IRF is a tri-phasic IRF if $abs(2MA-) >= 10\% \times (1MA+)$ and $(3MA+) >= 10\% \times abs(2MA-)$. The

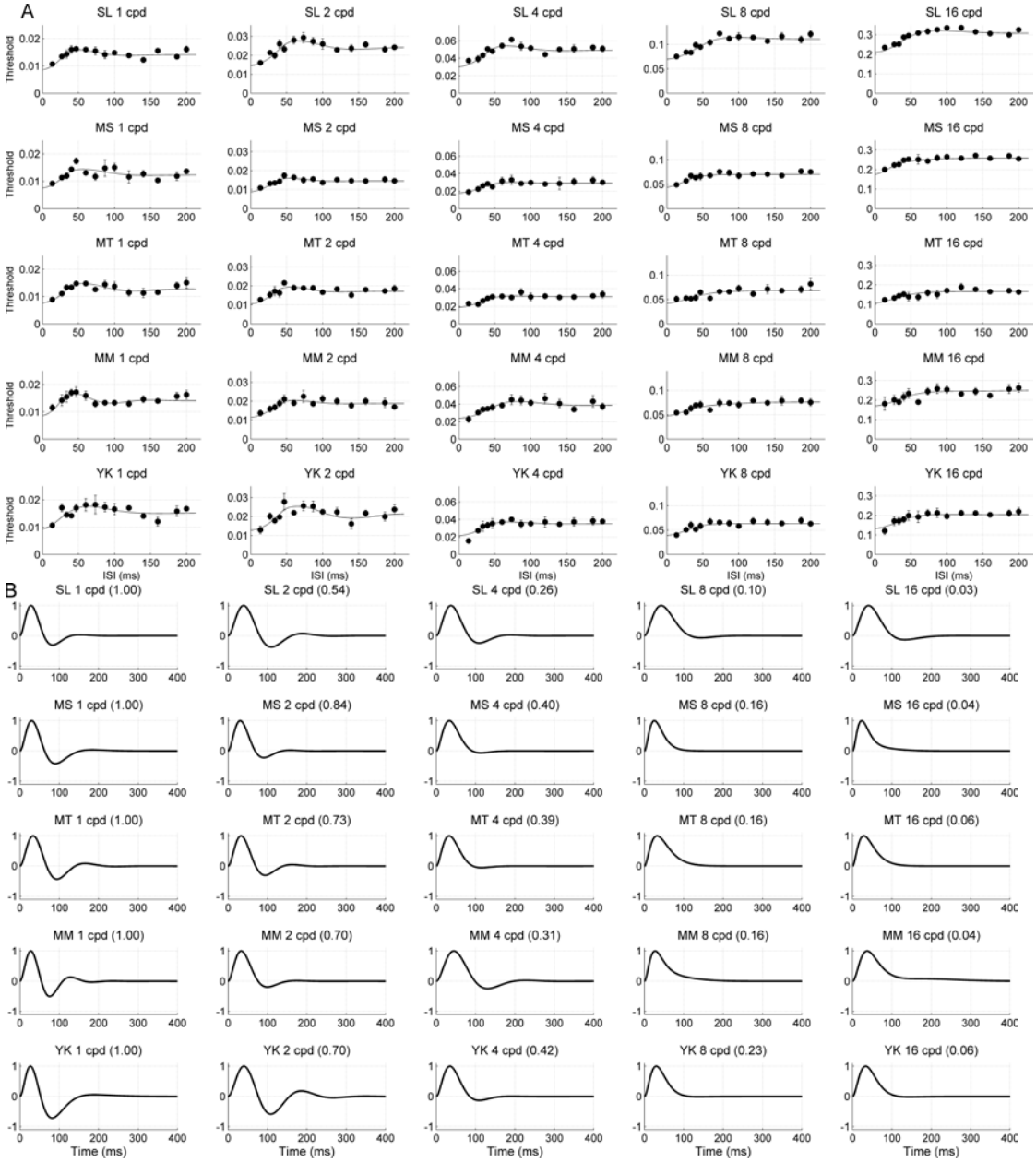

Figure 3.3: Thresholds (A) and IRFs (B) on all observers. The first to the fifth rows are for observers SL, MS, MT, MM, and YK, respectively. The first to the fifth columns are for spatial frequencies 1, 2, 4, 8, and 16 cpd respectively. A: Thresholds. Thresholds are the mean of 5 independent measurements (denoted by points with error bars) and model-thresholds (denoted by smooth curves) calculate from IRFs using the working model. Error bars indicate ± 1 SEM (some of error bars are smaller than the size of point). The abscissa is ISI in millisecond and the ordinate is log contrast energy threshold. B: IRFs. The abscissa is time in millisecond and the ordinate is the normalized amplitude of IRF without dimension. Observers' IRFs were normalized to their own 1 cpd IRFs respectively by a factor displayed on the title of the corresponding panel.

IRF is a bi-phasic IRF if $abs(2MA-) >= 10\% \times (1MA+)$ and $(3MA+) < 10\% \times abs(2MA-)$. The IRF is a mono-phasic IRF if $abs(2MA-) < 10\% \times (1MA+)$. '1MA+' means the maximum amplitude of the first (positive) phase. '2MA-' means the minimum amplitude of the second (negative) phase. '1MA+' means the maximum amplitude of the first positive phase. As showed in Table 3.1, all IRFs at the low spatial frequency (1 and 2 cpd) had two or three phases and most of IRFs at the high spatial frequencies (8 and 16 cpd) had one phase except observer SL's 16 cpd IRF had a weak second phase while observer SL's other spatial frequencies IRFs were tri-phasic IRFs. Observers MS and MT have the mono-phasic IRFs of 4 cpd while other observers have bi- or tri-phasic IRFs of 4 cpd.

3.3.2.2 Peak Time, Zero-crossing Time, and Amplitude of IRFs

I quantitatively compared six properties of IRFs directly obtained from the shape of each IRF: the peak time of the first (excitatory) phase (1PT+), the peak time of the second (inhibitory) phase (2PT-), the first zero-crossing time (1ZC), the time interval between 1PT+ and 1ZC (ΔPT), the maximum (positive) amplitude of the first (positive) phase (1MA+), and the maximum (negative) amplitude of the second (negative) phase (2MA-).

Figure 3.4 was the box plot of 1PT+, 2PT-, 1ZC, 1MA+, 2MA-, and ΔPT, which showed significant differences between lower spatial frequencies and higher spatial frequencies visually.

The p-values of the Wilcoxon rank-sum test also showed significant differences of 1ZC ($p = 0.0002$), 1MA+ ($p < 0.0002$), ΔPT ($p < 0.0002$) between the lower spatial frequencies and the higher spatial frequencies. The significant difference

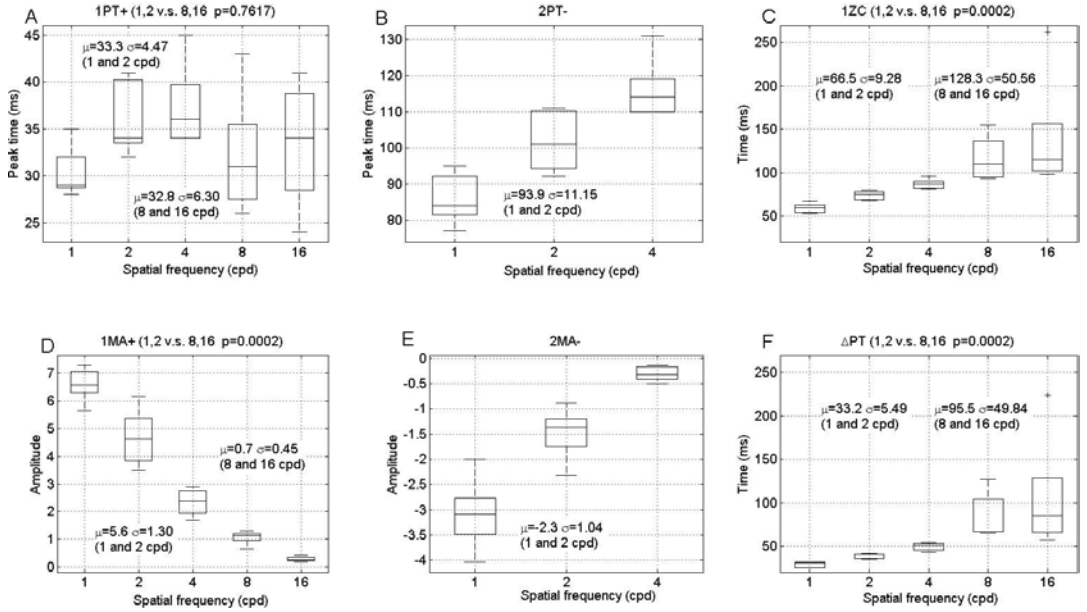

Figure 3.4: Box plots of the peak time of the first (excitatory) phase (1PT+) (panel A), the peak time of the second (inhibitory) phase (2PT-) (panel B), the first zero-crossing time (1ZC) (panel C), the maximum (positive) amplitude of the first (positive) phase (1MA+) (panel D), the maximum (negative) amplitude of the second (negative) phase (2MA-) (panel E), and the time interval between 1PT+ and 1ZC (ΔPT) (panel F). The box plot is a simplified visualization of the sample distribution. The top and the bottom of the box are the 25th and 75th percentiles of the samples respectively. The line in the middle of box is the sample median. The whiskers extend to the furthest observations. Observations beyond 1.5 times of the interquartile ranges are marked as outliers displayed with a '+' sign. The p-values of the Wilcoxon rank-sum test between lower spatial frequencies (1, 2, and 4 cpd) and higher spatial frequencies (8 and 16 cpd) are displayed on the title of the panel. The mean μ and the standard deviation σ of corresponding values of the lower spatial frequency and the higher spatial frequency are displayed nearby corresponding boxes. The abscissa is the spatial frequency in cpd and the ordinate are the peak time in millisecond (panel A, B, C, and F), and the amplitude (panel D and E). Panel B and E only include spatial frequencies 1, 2, and 4 cpd because the lack of the second phase of spatial frequencies 8 and 16 cpd IRFs in most cases.

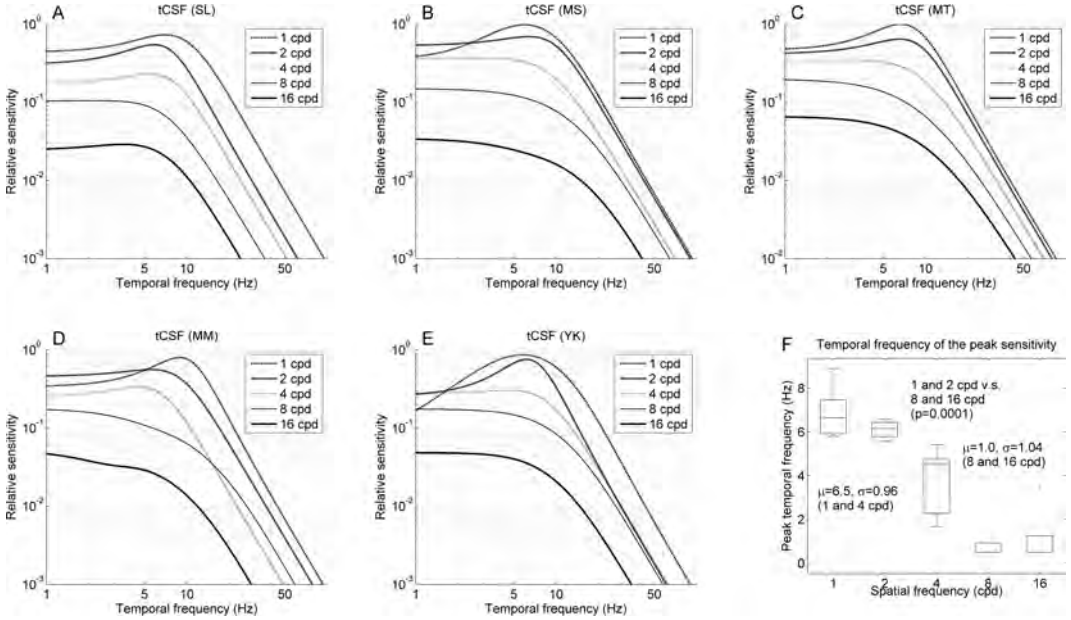

Figure 3.5: Temporal contrast sensitivity functions (tCSF). The tCSF was calculated from the IRF through the definition of the transform function of the linear system. Panels A, B, C, D, and E are observers SL, MS, MT, MM, and YK's tCSFs respectively. The abscissa is the temporal frequency (Hz) in log scale and the ordinate is the sensitivity (relative units) in log scale. Panel F is the box plot of the temporal frequency of the peak amplitude of all tCSFs. The minimum temporal frequency of the peak amplitude were set to 0.5 Hz when the temporal frequency is less than 0.5 Hz. The abscissa is the spatial frequency in cpd and the ordinate is the temporal frequency of the peak amplitude in Hz.

of 1PT+ was not detected ($p = 0.7617$).

The mean of 1ZC of the lower spatial frequencies and the higher spatial frequencies were 66.5 ± 9.28 and 128.3 ± 50.56 respectively. The mean of 1MA+ of the lower spatial frequencies and the higher spatial frequencies were 5.6 ± 1.30 and 0.7 ± 0.45 respectively. The mean of ΔPT of the lower and higher spatial frequencies were 33.2 ± 5.49 and 95.5 ± 49.84 respectively.

3.3.3 Temporal Contrast Sensitivity Function

The temporal contrast sensitivity functions (tCSF) that calculated from IRFs through the definition of the transform function (see equation 3.2) of the linear system showed in Figure 3.5. In equation 3.2, $G(q)$ is the transform function, $g(k)$ the impulse response function, $q = e^{iw\pi}, \quad w = 0, ..., 1$. The tCSF is plotted as $log(|G(e^{iw\pi})|)$ v.s. $log(e^{iw\pi}), \quad w = 0, ..., 1.$

$$G(q) = \sum_{k=1}^{\infty} g(k)q^{-k}, \quad (q = e^{iw\pi}, w = 0, ..., 1) \tag{3.2}$$

The tCSFs of the lower spatial frequencies (1 and 2 cpd) and the higher spatial frequencies (8 and 16 cpd) had different temporal frequency responses on all observers visually. The box plot of the temporal frequency of the peak amplitude of tCSFs also showed significant difference between the lower spatial frequency and the higher spatial frequency (see Figure 3.5F). The mean of the temporal frequency of peak amplitude of the tCSFs of the lower spatial frequency and the higher spatial frequency were 6.5±0.96 and 1.0±1.04 Hz respectively. The temporal frequency of peak amplitude of the tCSFs of the lower spatial frequency and the higher spatial frequency were significantly different (the Wilcoxon rank-sum test, p=0.0001).

Same with the IRF differences in the time domain, the different temporal frequency responses in the frequency domain also indicated different temporal characteristics between the low spatial-frequency-tuned channel and the high spatial-frequency-tuned channel.

3.4 Discussion

3.4.1 Spatial-Frequency-Tuned Channels

The spatial frequency stimuli in this study had ring-structure Fourier spectrum components at spatial frequencies 1, 2, 4, 8 and 16 cpd in all directions of the 2-D space (see Figure 3.1). As showed in Results, lower spatial frequencies (1 and 2 cpd) and higher spatial frequencies (8 and 16 cpd) had significantly different IRFs especially different phase. Spatial frequency 4 cpd was located between the lower- and higher-spatial frequencies and showed some border characteristics which will described later.

The Gaussian patch of 0 cpd used in Chapter 2 had a very low Fourier spectrum component. The IRFs of the 0 cpd were also compared with those of 1, 2, 4, 8, and 16 cpd of this chapter. As showed in Figure 3.6, all average IRFs of 0, 1, 2 cpd were tri-phasic IRFs (corresponding with the bandpass characteristics) while IRFs of 8 and 16 cpd were mono-phasic IRFs ($abs(2MA-) < 0.1 \times 1MA+$) (corresponding with the bandpass characteristics). It indicated that at least two kinds of spatial-frequency-tuned channels, the lower- (bandpass) and higher- (low-pass) spatial-frequency-tuned channels that dominates the lower spatial frequencies (0, 1, and 2 cpd) and the higher spatial frequencies (8 and 16 cpd), respectively, exists in human vision.

Although the 1PT+, 2PT-, 1ZC, and 1MA+ of 0 cpd were different from those of 1 and 2 cpd, average IRFs of 0, 1, and 2 cpd were all tri-phasic IRFs (see Figure 3.6). The stimuli of 0 cpd were the positive- or negative-contrast Gaussian patch which only included either positive- or negative-contrast component while the stimuli of 1 and 2 cpd had a positive centre and negative surround structure.

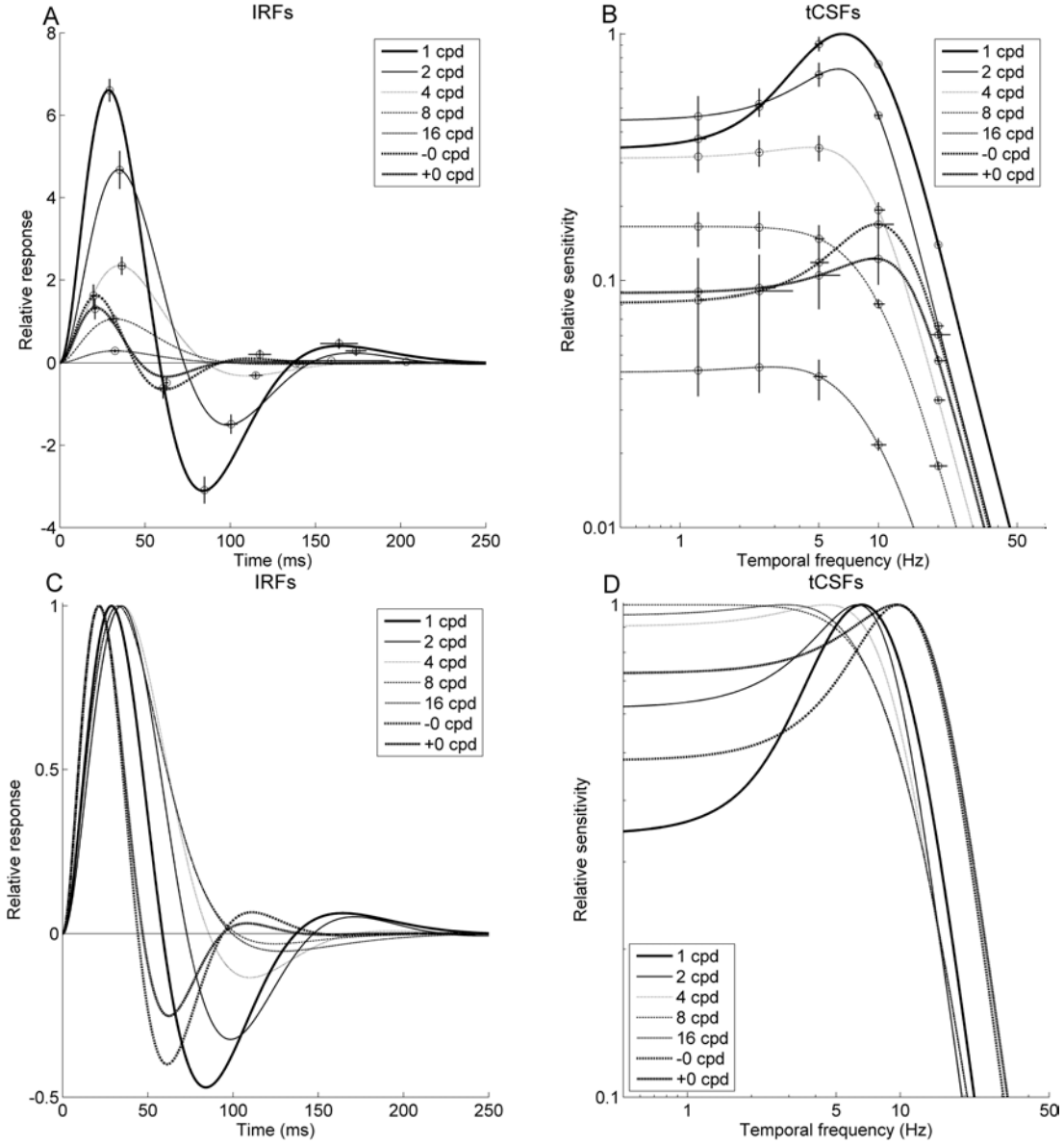

Figure 3.6: Average IRFs (panel A), corresponding tCSFs (panel B), normalized average IRFs (panel C), and normalized tCSFs (panel D). Data come from five observers' IRFs at 0, 1, 2, 4, 8, and 16 cpd. The positive- and negative-contrast IRFs of 0 cpd were came from the experiment using Gaussian patch in Chapter 2. Various style lines denote 0, 1, 2, 4, 8, and 16 cpd respectively. Panel A includes IRFs of spatial frequencies 0, 1, 2, 4, 8, and 16 cpd. The error bars at peak points denote ±1 S.E.M. . The abscissa is time in millisecond and the ordinate is the relative response. Panel B includes tCSFs derived from corresponding IRFs. The error bars at 1.25, 2.5, 5, 10, and 20 Hz denote the variation range of tCSFs at corresponding points. The abscissa is the temporal frequency in Hz and the ordinate is the relative sensitivity. '+0' and '-0' donate positive- and negative-contrast IRFs or tCSFs of 0 cpd respectively.

The difference between 0 and 1, 2 cpd was possibly originated from the centre-surround latency which was about 3-8 ms reported by Lee and Smith [Lee et al., 1989; Smith et al., 1992]. The 3-8 ms latency was close to 6-10 ms interval between the first peak time of 0 and 1 cpd which were measured in this study.

At the same time, the difference between IRFs of 0 cpd and 1, 2 cpd caused different peak temporal sensitivity, about 10 and 7 Hz respectively. This difference extended the range of temporal sensitivity and should be important to the motion sensitivity which was discussed later.

The 4 cpd spatial frequency showed some transitionary characteristics between 1, 2 cpd and 8, 16 cpd on both the phase of IRF and the peak sensitivity of tCSF. For observer SL and MM, the 4 cpd IRFs (bi-phasic) and tCSF (bandpass) were more similar with those of 1 and 2 cpd than those of 8 and 16 cpd. For other observers, the 4 cpd IRFs (very weak second phase) and tCSF (low-pass) were more similar with those of 8 and 16 cpd than those of 1 and 2 cpd.

The border between the lower-and higher-spatial-frequency-tuned channels should be around 4 cpd spatial frequency while the individual difference among various observers exist. The transitionary instead of transilient border between the lower- and higher-spatial-frequency-tuned channels was reasonable because the visual system is a complex neural network although parts of system showed different characteristics while processing different spatial frequencies. Furthermore, the transitionary border can not cause some kind of temporal sensitivity 'ditch' nearby the border.

The tCSFs of this study were consistent with Kelly's measurement results with traveling-wave stimuli using stabilizing retinal images technology [Kelly, 1979]. The corresponding tCSF can be obtained by fixing spatial frequency in

the FIG.13 or FIG.15 of Kelly [1979]. The tCSFs of spatial frequencies 8 and 16 cpd in FIG.13 or FIG.15 were also low-pass and the CSFs of spatial frequencies 1 and 2 cpd were bandpass. Both of peak sensitivities of those tCSFs were similar with those of tCSFs of this study.

3.4.2 Spatial-Frequency-Tuned Channels and the M and P Pathways

Following discussion showed that the M- and P-pathways in human visual system dominated the detection of the lower spatial frequencies (0, 1, and 2 cpd) and the higher spatial frequencies (8 and 16 cpd), respectively, in the present study.

Firstly, larger receptive field of the Magno-cellular(M)-pathway and smaller receptive field of the Parvo-cellular(P)-pathway provided the neural basic of the lower- and higher-spatial-frequency-tuned channels.

Secondly, phasic and tonic response to light steps of the M- and P-pathway [Kaplan, 2004] and reports of tri-phasic IRFs in some M-ON cells with low spatial frequency but not with high spatial frequency [Benardete, 1994] were consistent with most of multi-phasic IRFs of the lower spatial frequencies and mono-phasic IRFs of the higher spatial frequencies.

Thirdly, faster conduction velocity of axons of the M-pathway than that of the M-pathway [Kaplan, 2004] which were consistent with earlier first zero-crossing time of the lower spatial frequencies than those of the higher spatial frequencies.

Fourthly, the M-pathway with high luminance contrast gain and the P-pathway with low luminance contrast gain [Kaplan and Shapley, 1986] which were consistent with the result that lower thresholds and higher first-phase-positive-amplitude

(1MA+) (higher sensitivity) of the lower spatial frequencies and higher thresholds and lower 1MA+ (lower sensitivity) of the higher spatial frequencies, respectively.

3.4.3 Comparison with Results of Local Spatial Channels

Kontsevich and Tyler [Kontsevich and Tyler, 2013] measured the masking sensitivity curves of local spatial channels using Gaussian test stimuli to probe low frequency channels and using Gabor test stimuli to probe high frequency channels. Their results showed that the peak masking sensitivity of the low spatial frequency channels were ranged between 1 and 3 cpd among various observers and various eccentricity (see Figure 3 of their literature) and those of the high spatial frequency channels were ranged between 6 and 9 cpd (see Figure 4 of their literature). Their results were consistent with my results of the lower- (1 and 2 cpd) and higher- (8 and 16 cpd) spatial-frequency-tuned channels although totally different measurements in corresponding experiments.

3.4.4 Motion Model

Some researches in motion perception suggest that motion detection for different size of dot stimuli can be explained by only one single low-pass spatial filter [Morgan, 1992; Morgan and Mather, 1994], but there is a motion type that cannot be explained by the single filter [Bex et al., 1995].

In Watson and Ahumada's model of human visual-motion sensing [Watson and Ahumada, 1985], two different temporal impulse responses of the scalar motion sensor were needed. In their model, one impulse response was tri-phasic and another impulse response was bi-phasic.

Adelson and Bergen's spatiotemporal energy models for the perception of motion [Adelson and Bergen, 1985] also needed two different temporal impulse responses.

Above models showed that both the different impulse responses between the lower- and higher-spatial-frequency-tuned channels and inside the lower-spatial-frequency-tuned channel are essential to the motion perception of human vision, which is mainly mediated by M-pathway.

3.4.5 Spatial Frequency and Spatial Structure

The spatial frequency was defined as an oscillation of luminance or color in space by De Valois [De Valois and De Valois, 1990]. The spatial frequency is usually measured by the repeat of sinusoidal components which is determined by the Fourier transform.

Figure 3.7 showed the stimuli and corresponding Fourier spectrum in Chapter 2 and Chapter 3. Labels '0+1', '0+2', '0+4', '0+8', and '0+16' indicated stimuli with spatial structures 0, 1, 2, 4, 8, and 16 cpd used in the positive- and negative-contrast detection experiment in Chapter 2. The term 'spatial structure' was used for the stimuli because Fourier spectrum of the stimuli images included relatively-large low spatial frequency components although the stimuli had circular spatial structures in various spatial sizes. In term of spatial frequency, the stimuli labelled with 0, '0+1', '0+2', '0+4', '0+8', and '0+16' had very low spatial frequency components. Stimuli of spatial frequencies 1, 2, 4, 8, and 16 cpd were used in the study of this chapter. The stimuli had a circular structure Fourier spectrum in that the very low spatial frequency component did not exist.

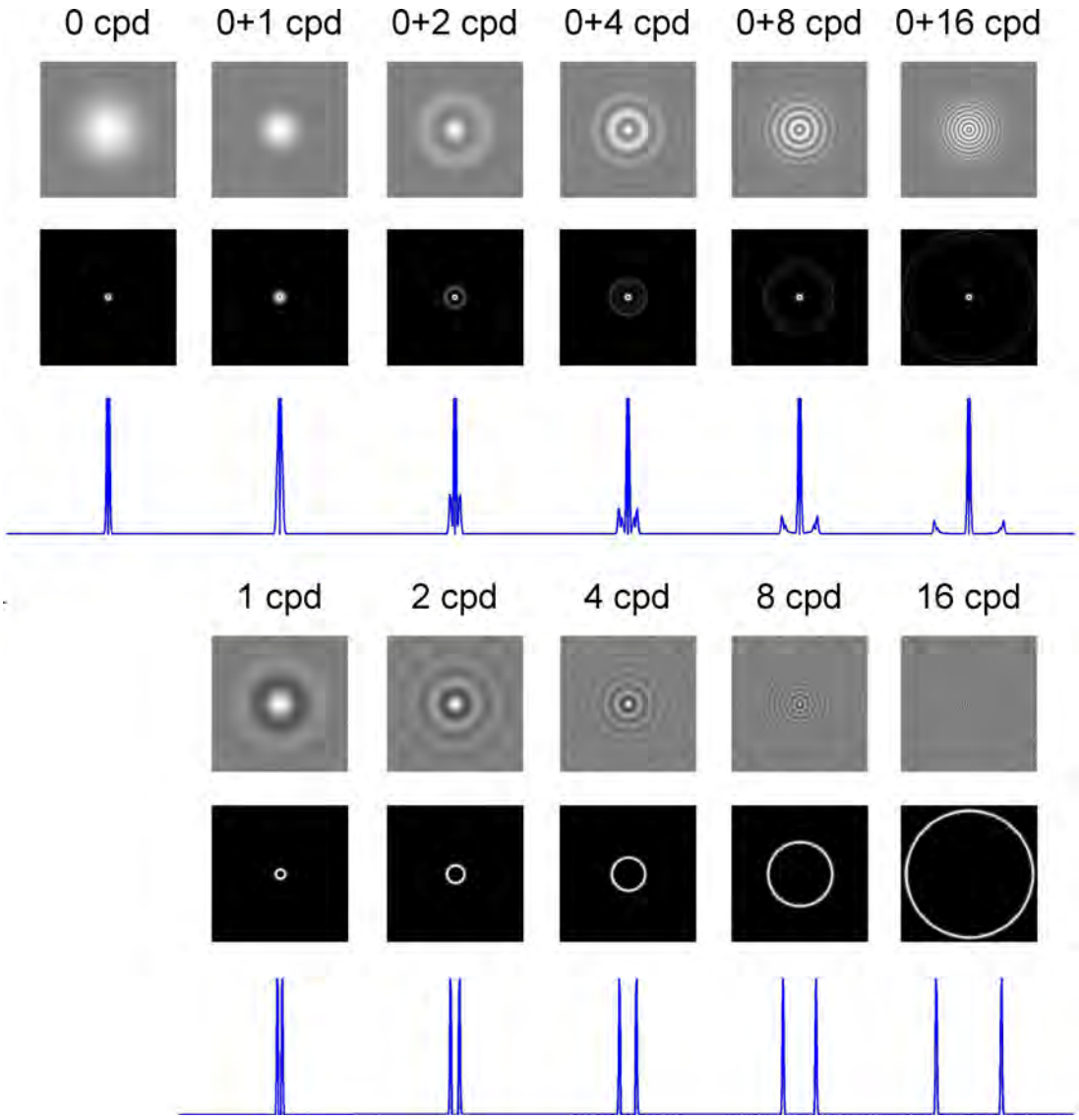

Figure 3.7: Fourier spectrum of stimuli in terms of spatial structure and spatial frequency. The first row shows the positive stimuli with spatial structures 0, 1, 2, 4, 8, and 16 cpd in positive- and negative-contrast detection experiment, which has titles '0+1', '0+2', '0+4', '0+8', and '0+16'. The second row is the Fourier spectrum of the stimuli showed in the first row. The third row is the profile of the second row. Only positive contrast stimuli are showed here because the Fourier spectrum of the negative contrast stimuli are identical to those of positive contrast stimuli. The fourth row shows the stimuli in the spatial-frequency-tuned channel experiment. The fifth row is the Fourier spectrum of the stimuli showed in the fourth row. The sixth row is the profile of the fifth row. The DC parts are not showed in above Fourier spectrum.

Comparing the results of Chapter 2 and Chapter 3, I found the the reason why the stimuli used in Chapter 2 did not 'hit' the corresponding spatial-frequency-tuned channels was the low spatial frequency component dominated the detection of the stimuli used in Chapter 2. In other words, the spatial-frequency-tuned channels were 'spatial-frequency-tuned' instead of 'spatial-structure-tuned'. The peripheral inhibition of receptive field played an important role in the difference between spatial frequency and spatial structure.

3.5 Conclusion

At least two kinds of spatial-frequency-tuned channels, the lower- and higher-spatial-frequency-tuned channels that dominates the lower spatial frequencies (0, 1, and 2 cpd) and the high spatial frequencies (8 and 16 cpd), respectively, exists in human vision. The lower-spatial-frequency-tuned channel is bandpass and the higher-spatial-frequency-tuned channel is low-pass.

In high possibility, the M- and P-pathways in human visual system dominated the lower spatial frequencies (0, 1, and 2 cpd) and the higher spatial frequencies (8 and 16 cpd), respectively, in the present study.

Chapter 4

Other Things

This chapter includes estimating of the psychometric function using the extreme value distribution function, the display model, and the comparison of the staircase method and the psi method.

4.1 Psychometric function

The psychometric function describes the relationship between the physical intensity of stimuli and the observers' responses. In a detection task, the observers' responses are described by the possibility of seeing the stimulus. The Weibull distribution [Weibull, 1951] was used to describe the psychometric function [Green and Luce, 1975; Watson, 1979]. However, I found that the extreme value distribution can describe the psychometric function better and has a 'psychophysics meaning' that can explain why the extreme value distribution is better.

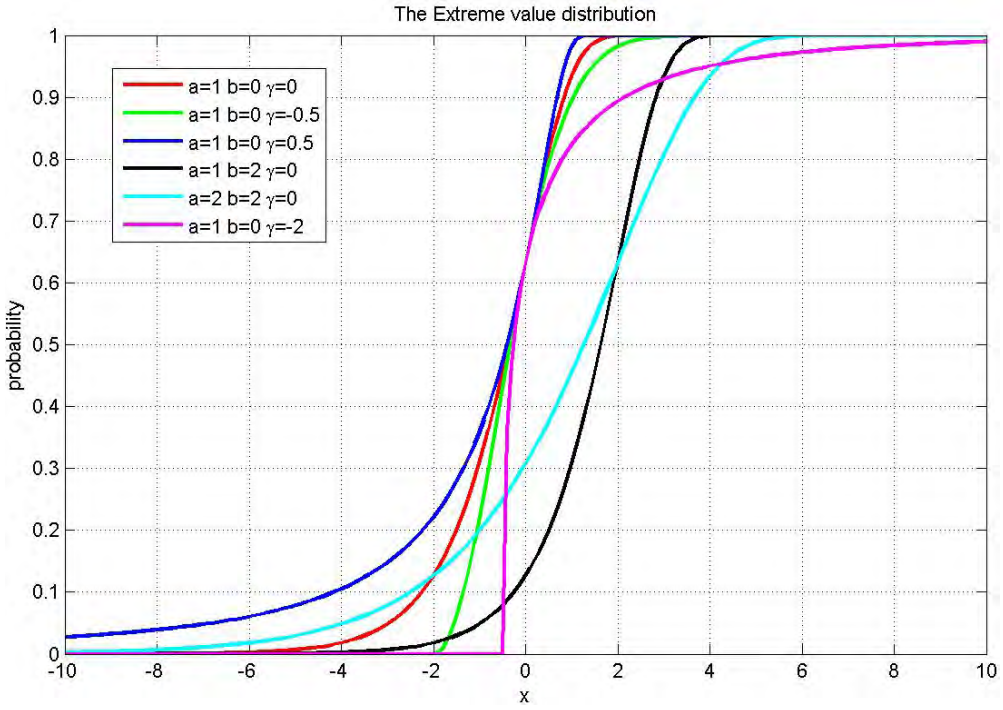

Figure 4.1: The cumulative distribution function of the extreme value distribution. Color curves indicated the cumulative distribution function with various parameters.

4.1.1 The Extreme Value Distribution

The central limit theory is concerned with the limit of the sums of random variables $X_1+X_2+\ldots+X_n$ as $n \to \infty$, whereas the extreme value theory is concerned with the limit of the $\max(X_1, X_2, \ldots, X_n)$ or $\min(X_1, X_2, \ldots, X_n)$ as $n \to \infty$.

$$G(x) = 1 - \exp\left(-\left(1+\gamma\frac{-x-b}{a}\right)^{-\frac{1}{\gamma}}\right), \quad 1+\gamma\frac{-x-b}{a} > 0 \tag{4.1}$$

The cumulative distribution of the extreme value distribution has a form showed in Equation 4.1 (in case of $\min(X_1, X_2, \ldots, X_n)$). a is the scale parameter. b is the position parameter. γ is the shape parameter which indicate different types of distributions [de Hann and Ferreira, 2006]. It is the *Fréchet* class of dis-

tributions when $\gamma > 0$. It is the Gumbel distribution when $\gamma = 0$. It is the reverse-Weibull class of distributions when $\gamma < 0$. Figure 4.1 shows samples of the cumulative distribution of the extreme value distribution.

4.1.2 Psychophysics Meaning

Let random variables $X_i(i = 1, \ldots, n)$ correspond to the sample space $\{x_i\}$. x_i is the intensity value which the stimulus can be detected by the i_{th} detector (or reason). The probability that the stimulus can be detected by at least one detector at intensity x is

$$P(min(X_1, X_2, \ldots, X_n) \leq x)$$

According to the extreme value theory (see [de Hann and Ferreira, 2006] for more detail),

$$\lim_{n \to \infty} P(min(X_1, X_2, \ldots, X_n) \leq x) = G(x)$$

The form of $G(x)$ see Equation 4.1 which is the min form of the extreme value distribution. The random variable

$$min(X_1, X_2, \ldots, X_n)$$

obeys the extreme value distribution when $n \to \infty$. In another words, $G(x)$ is the probability that the stimulus can be detected at intensity x by at least one detector when the count of detectors tends to infinity.

The reason, why the Weibull distribution was used, is that it is the most simple function satisfying the distribution function condition [Weibull, 1951]. The

Weibull distribution is a specific case of the extreme value distribution when the shape parameter $\gamma < 0$.

4.1.3 Estimation of Psychometric Function

Psychometric functions were estimated using the reverse form of cumulative distribution function of the extreme value distribution (See Equation 4.1). The extreme value distribution has three parameters, a, b, and γ. Parameters a and b are the slope and the threshold. Parameter γ is for different types of distributions.

Observers' responses were counted separately grouped by correct answers and wrong answers in continual intervals at intensity axis. The percentages of correct answers and wrong answers were calculated at each interval. The count of correct answers was cumulated among the positive direction of the intensity axis and the count of wrong answers was cumulated among the negative direction of the intensity axis. The psychometric function was estimated from the percentage data using a least-squares method. The threshold value is the parameter b which corresponds about 63.21% of correct answer. The slope value is the parameter a.

Figure 4.2 showed some sample fittings using the extreme value distribution function. In the cases of $\gamma \geq 0$, measured data can not be fitted better using the Weibull distribution function.

Figure 4.3 showed the histogram of the parameters of positive- and negative-contrast detection and spatial-frequency-tuned detection. Most of values of parameter γ were less than 0 which corresponded to the Weibull distribution. The other values of parameter γ were ≥ 0 which corresponded to the reverse form of the *Fréchet* distributions and the Gumbel distribution. In cases of $\gamma \geq 0$,

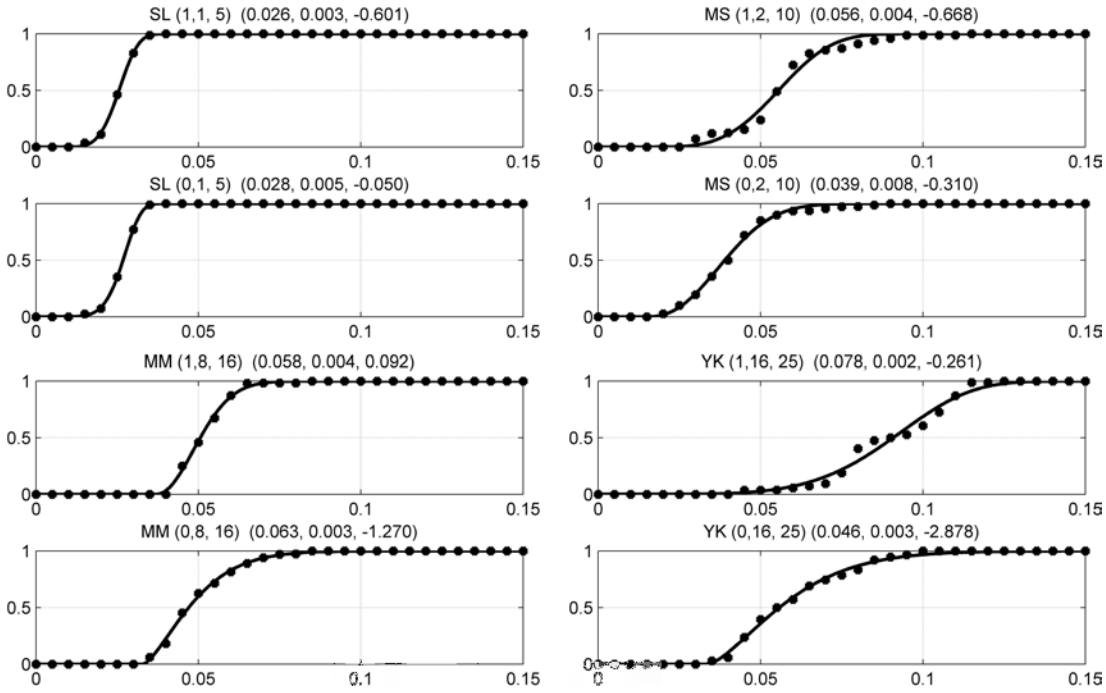

Figure 4.2: Psychometric functions and percentages of correct answers. The x-axis is the intensity of the stimulus in log contrast energy scale. The y-axis is the percentages of correct answers. Title 'SL (1,1, 5) (0.026, 0.003, -0.601)' means observer SL's positive contrast, 1 cpd, ISI=5 frames, $b = 0.026$, $a = 0.003$, and $\gamma = -0.601$.

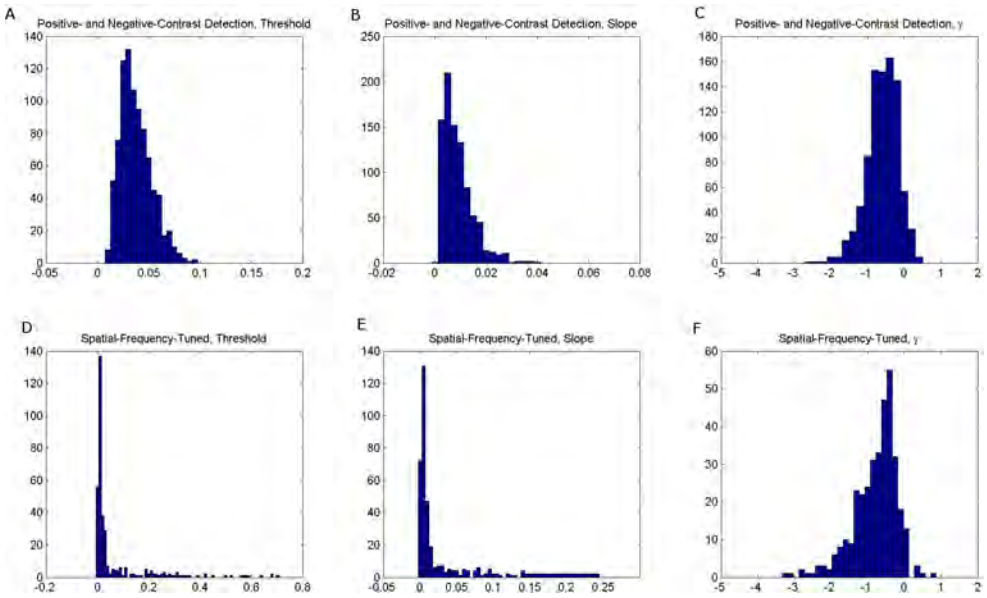

Figure 4.3: The histogram of the parameters of positive- and negative-contrast detection and spatial-frequency-tuned detection. Data is from the experiments described in chapters 5, 6, and 7. The parameters are estimated by the psychometric function in form of the extreme value distribution. The first row is for positive- and negative-contrast detection and the second row is for spatial-frequency-tuned detection. A, threshold. B, slope. C, parameter γ. D, threshold. E, slope. F, parameter γ.

the extreme value distribution can describable the data better than the Weibull distribution.

4.2 Display model

A display model was built to generate accurate luminance and chromatic coordinate values on the display. The error rate of CIE (x,y,L) values were less than 3% using the display model with a CRT display controlled by the VSG system.

Figure 4.4: The flowchart of the kernel procedure xyL2Vrgb. The expectative luminance and chromatic coordinate (x,y,L) is transformed into the control values of three guns of the CRT (vr,vg,vb).

4.2.1 Elements of the model

The kernel of the model was the procedure $xyL2Vrgb$ which calculated the control values of three guns of CRT from the expectative (x,y,L) value. Figure 4.4 showed the flowchart of the kernel procedure $xyL2Vrgb$.

The (x,y,L) was transformed into (X,Y,Z) through the following formulas.

$$X = \frac{x}{y}L$$

$$Y = L$$

$$Z = \frac{1-x-y}{y}L$$

The (X,Y,Z) was transformed into (R,G,B) by

$$\begin{pmatrix} R \\ G \\ B \end{pmatrix} = \begin{pmatrix} a_{1,1} & a_{1,2} & a_{1,3} & a_{1,4} & a_{1,5} & a_{1,6} & a_{1,7} & a_{1,8} & a_{1,9} & a_{1,10} \\ a_{2,1} & a_{2,2} & a_{2,3} & a_{2,4} & a_{2,5} & a_{2,6} & a_{2,7} & a_{2,8} & a_{2,9} & a_{2,10} \\ a_{3,1} & a_{3,2} & a_{3,3} & a_{3,4} & a_{3,5} & a_{3,6} & a_{3,7} & a_{3,8} & a_{3,9} & a_{3,10} \end{pmatrix} \begin{pmatrix} 1 \\ Z \\ Y \\ X \\ YZ \\ XZ \\ XY \\ Z^2 \\ Y^2 \\ X^2 \end{pmatrix}$$

. The matrix A was the transform matrix which will be estimated from measured data.

The procedure *RevGamma* was a reverse Gamma procedure which checked a Gamma dictionary to get the correspond value. A linear insertion point was gotten if item was not found in the dictionary. The *RevGamma* supported non-linear Gamma functions.

4.2.2 Parameters estimation and calibration

The Gamma dictionary were measured by the CS-200 controlled by a program automatically. The program displayed stimuli on the screen of CRT and controlled the CS-200 to measure the correspond (x,y,L) value. The measurement included following configurations.

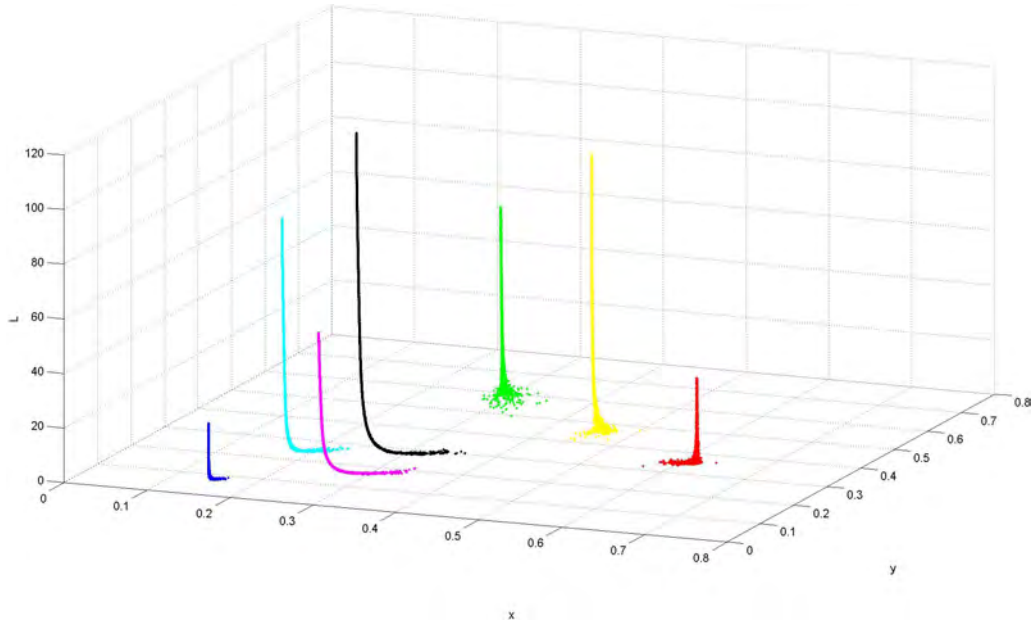

Figure 4.5: Measurement data of R, G, and B guns of G500 in 3D space. Data is from 2048×7 measurements of CRT display (CPD G500, SONY). The x-axis is the CIE chromatic coordinate x. The y-axis is the CIE chromatic coordinate y. The z-axis is the CIE luminance coordinate L (cd/m^2). Color points indicate correspond gun or guns together. Black points indicate R, G, and B guns together.

- R gun only
- G gun only
- B gun only
- R and G guns together
- R and B guns together
- G and B guns together
- R, G and B guns together
- maximum R gun, and change G and B guns together
- maximum G gun, and change R and B guns together
- maximum B gun, and change R and G guns together
- randomize R, G, and B gun

Each configuration item above was measured in $2^{11} = 2048$ steps. The measurement of the first three items generated the Gamma dictionary. Figure 4.5 showed a part of measurement data of CPD-G500 CRT.

The parameter matrix A was estimated by the $nlinfit$ function provided by Matlab using above measurement data. The parameter matrix which I used in the experiment was listed below.

$$A' = \begin{pmatrix} 0.0378640475004 & 0.0277607870369 & 0.0498334124299 \\ -0.107813525679 & 0.0238515357108 & 0.0845831302281 \\ -0.307970317531 & 1.32024926101 & -0.0166949996491 \\ 0.714496806732 & -0.721473183762 & 0.00458798900889 \\ 1.32171123566e-05 & 9.16550151932e-07 & -8.39973885568e-07 \\ -3.50598099590e-05 & -9.59914314205e-06 & 7.10510835252e-06 \\ -0.000158054348075 & 0.000104068453633 & 1.34888190212e-05 \\ 5.17797996435e-07 & 4.82658718454e-06 & -2.01838884209e-06 \\ 6.24592835946e-05 & 3.23370199539e-05 & -1.13576092229e-05 \\ 0.000165993018057 & -7.28871521252e-05 & -4.52803540123e-06 \end{pmatrix}$$

4.2.3 Model test

The error rate of (x,y,L) was less than 3%. The error rate was calculated by

$$error\_rate = \frac{expected\_value - measured\_value}{expected\_value} \times 100$$

2000 random points were measured to test the display model. Figure 4.6 showed the results.

4.3 Comparison of the staircase and psi method

An control experiment was done to compare the staircase method and the psi method. The detection thresholds of double pulses separated by 14 ISIs (0, 6.7, 13.3, 20.0, 26.7, 33.3, 40.0, 46.7, 53.3, 60.0, 66.7, 86.7, 106.7, and 133.3 msec, in

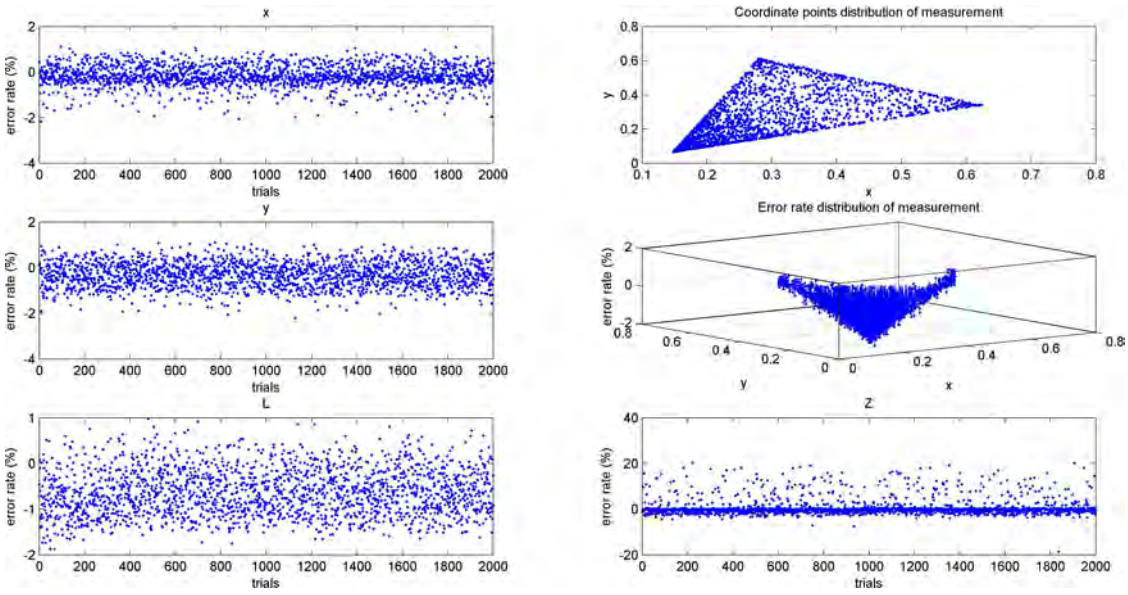

Figure 4.6: Results of model test. Data is from 2000 random measurements from the CRT display by the CS-200. A, the error rate of CIE coordinate x. The x-axis is the trial number and the y-axis is the error rate of CIE coordinate x in percentile. B, the error rate of CIE coordinate y. The x-axis is the trial number and the y-axis is the error rate of CIE coordinate y in percentile. C, the error rate of CIE coordinate L. The x-axis is the trial number and the y-axis is the error rate of CIE coordinate L in percentile. D, The CIE coordinate points distribution of measurement. The x-axis is the CIE coordinate x and the y-axis is the CIE coordinate y. E, The error rate distribution of measurement. Length of Lines indicate the error rates. The x-axis is the CIE coordinate x. The y-axis is the CIE coordinate y. The z-axis is the error rate in percentile. F, the error rate of CIE coordinate Z. The x-axis is the trial number and the y-axis is the error rate of CIE coordinate Z in percentile.

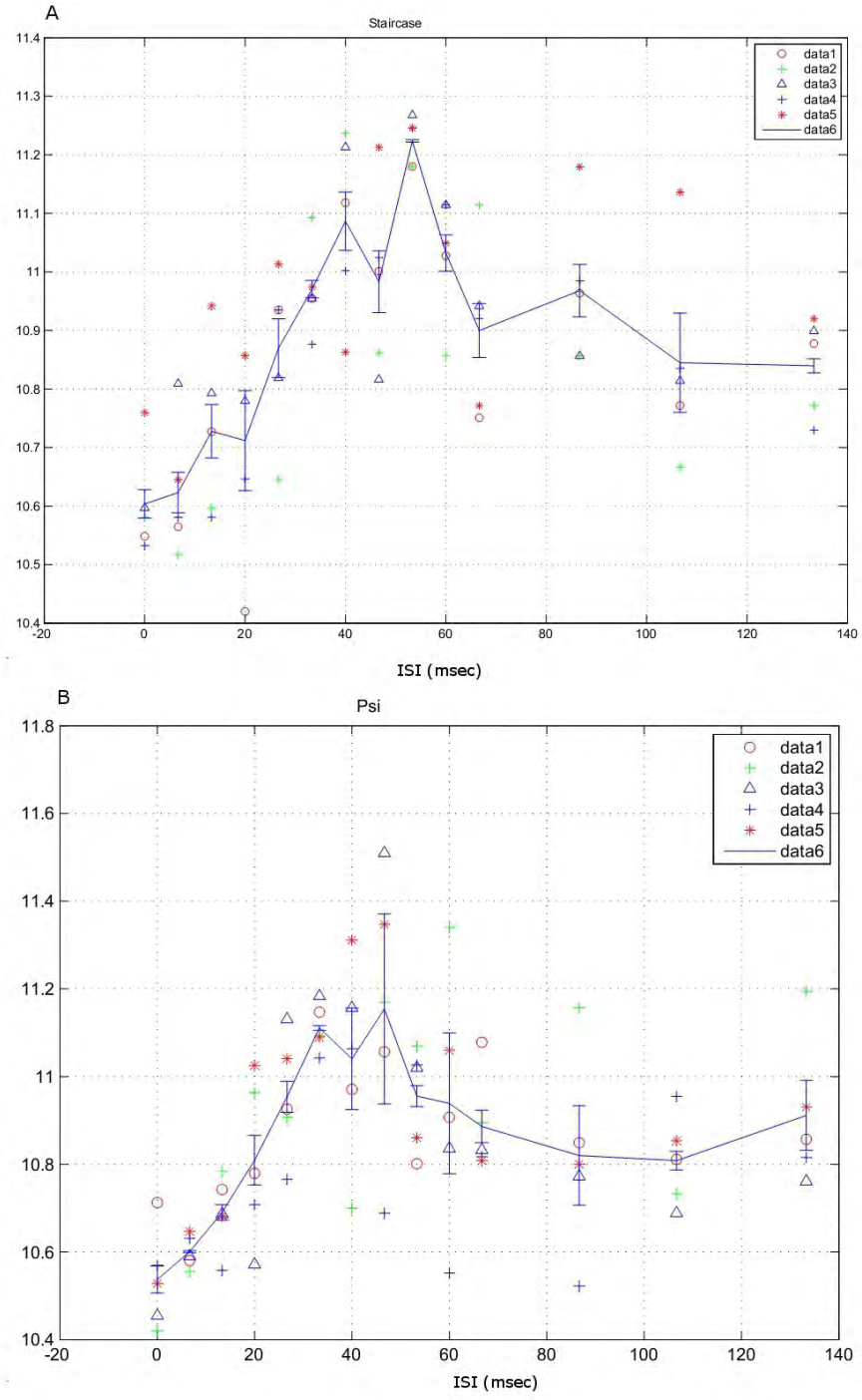

Figure 4.7: Thresholds estimated by the staircase method (panel A) and the psi method (panel B). Data is from five independent measurement in 14 ISIs setting for both staircase and psi method. Points come from different measurements are marked with different color and shape. The abscissa is ISI in millisecond and the ordinate is the threshold in cd/m^2 which is the peak amplitude of luminance of the stimulus. Error bars showed 1 SEM. Blue lines indicate the mean of the thresholds.

comparing item	the psi method	the staircase method	p value
threshold	0.0362 ± 0.0093	0.0367 ± 0.0083	0.6997
threshold deviation	0.0062 ± 0.0033	0.0050 ± 0.0017	0.2062
count of trials	20	22.4 ± 4.07	0.0000
count of turning points	7.7 ± 1.57	6	0.0000

Table 4.1: The comparison between the psi method and the staircase method.

terms of number of frames, 0, 1, 2, 3, 4, 5, 6, 7, 8, 9, 10, 13, 16, and 20 frames (6.7 msec/frame), ISI=0 means single pulse) were measured in the Gaussian patch stimulus by both the staircase method and the psi method. Five independent measurements were gotten for each threshold. Two methods were used alternately in three days experiment. Thresholds were showed in Figure 4.7. Table 4.1 showed the results of comparison.

The mean and the standard deviation of thresholds in all case of ISI were similar between two methods. The mean thresholds measured by the psi method was 0.0362 ± 0.0093. The mean thresholds measured by the staircase method was 0.0367 ± 0.0083. The statistic value p of paired t-test between two methods was 0.6997 which indicated no significant difference between thresholds measured by two methods.

The mean of threshold deviation (showed as the error bars at each threshold at certain ISI) of the psi method and the staircase method were 0.0062 ± 0.0033 and 0.0050 ± 0.0017. The paired t-test showed thresholds deviation of two methods were not significantly different ($p = 0.2062$).

The mean of count of trials included in one session of the staircase method was 22.4 ± 4.07. The psi method had a pre-set value, 20. The count of trials included in one session of the staircase method was significantly bigger than that of the psi method (paired t-test, $p \leq 0.0000$). It indicated that the count of trials

included in one session of the staircase method was significantly bigger than that of the psi method.

The mean of count of turning point included in one session of the psi method was 7.7 ± 1.57. The count of turning point included in one session of the staircase method was set to 6. The count of turning point of the psi method was significantly bigger than that of the staircase method (paired t-test, $p \leq 0.0000$). It indicated that the count of turning-points included in one session in the psi method was significant bigger than that of the staircase method.

Above results showed that the psi method is more efficient than the staircase method while both methods can get similar thresholds with similar deviation.

4.4 Fourier-Spectrum Contrast

A new definition of contrast, Fourier-spectrum contrast, is introduced here.

The intensity I_T of the stimulus was defined by the following equation.

$$I_T = max(dDC(fft(L(x, y))))$$

$L(x, y)$ is the luminance of the stimulus. dDC is the operator which delete the DC part of the spectrum. fft is the operator of 2-d Fourier transform.

The background intensity I_B was defined by the following equation.

$$I_B = DC(fft(L(x, y)))$$

DC is the operator which get the DC part of the spectrum.

The Fourier-spectrum-contrast C_F was defined by the intensity I_T against the

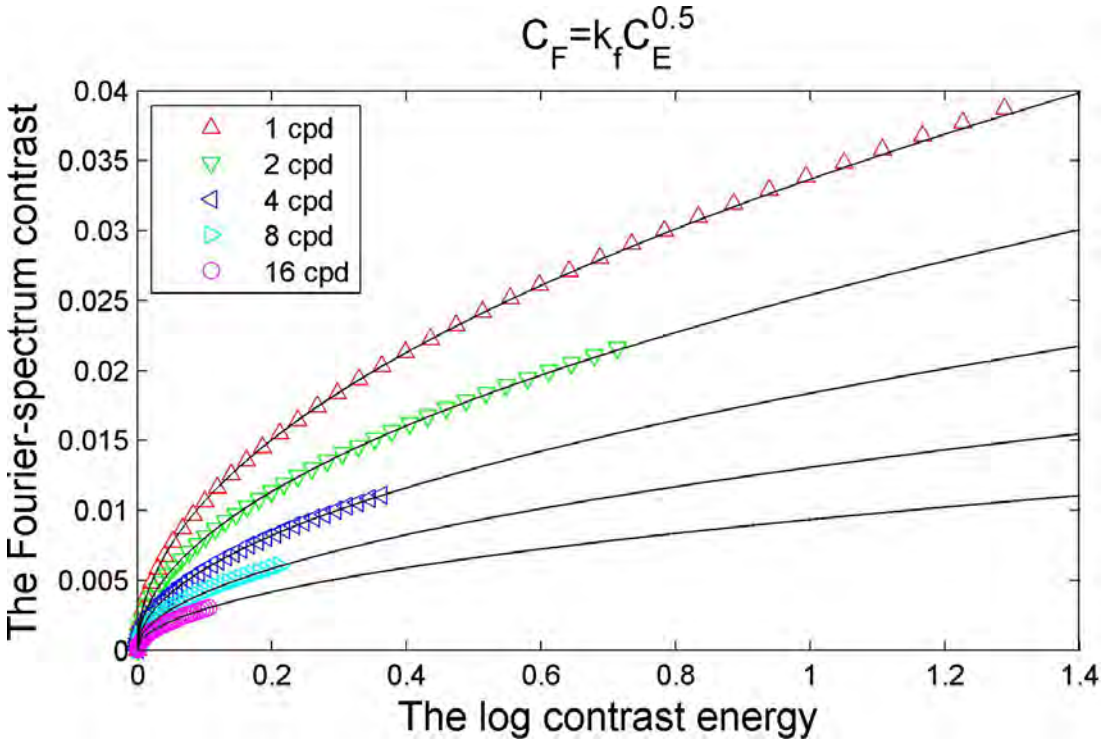

Figure 4.8: The relationship between the log contrast and the Fourier-spectrum contrast. Different shape points indicate the data points which calculated by the definition of the Fourier-spectrum contrast. The smooth curves are plotted using the experiential formula $C_F = k_f C_E^{0.5}$.

background intensity I_B as following.

$$C_F = \frac{I_T}{I_B}$$

I calculated the Fourier-spectrum contrast of the stimuli which used in Chapter 3. An experiential formula was divided as following.

$$C_F = k_f C_E^{0.5}$$

k_f is the factor of spatial frequency. The values of k_f are 0.03369 (1 cpd), 0.02541 (2 cpd), 0.01838 (4 cpd), 0.01308 (8 cpd), and 0.00935 (16 cpd) respectively.

Figure 4.8 showed the relationship between the log contrast energy and the Fourier-spectrum contrast.

4.5 Simulation of Eye Movement Effect

On consideration of possible effect by the eye movement during the displaying of double pulses, a simulation calculation has been done to evaluate the variation of the stimuli contrast when the double pulses have a spatial position offset.

The Gabor stimuli was compared with the stimuli used in the positive- and negative-contrast detection and the spatial frequency stimuli detection experiments on the log contrast, the log contrast energy, and the the Fourier-spectrum contrast.

The variation of the stimuli contrast was calculated by combining two stimuli with a spatial position offset defined by two parameters, Δd and θ. The Δd was the distance between two center of stimuli and was ranged between 0 and 0.5

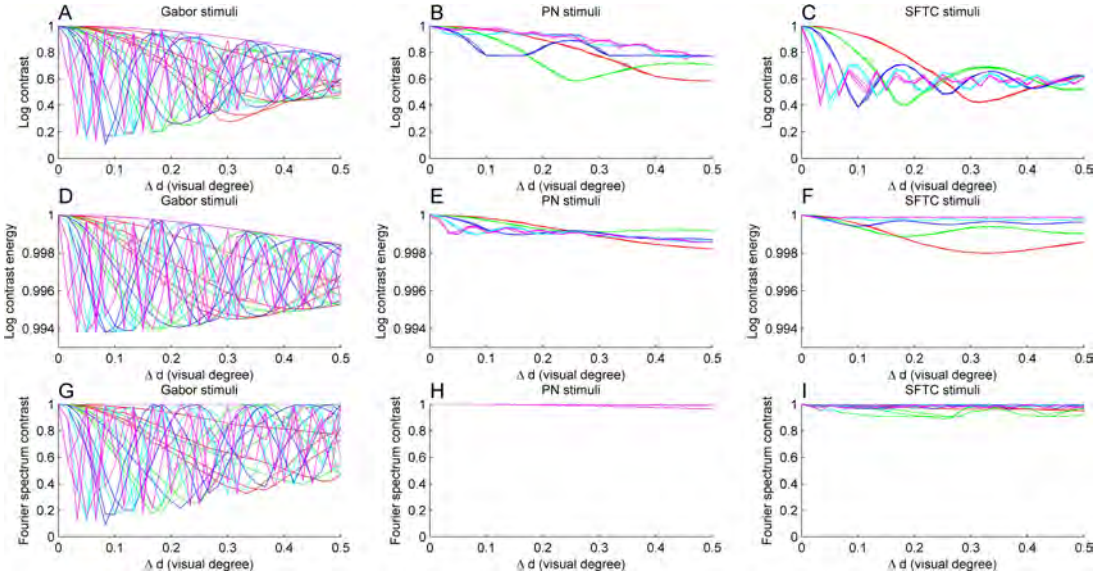

Figure 4.9: The simulation effect of contrast variation caused by eye movements. The first column of panels, panel A, D, and G, are for the variation curves of the Gabor stimuli. The second column of panels, panel B, E, and H, are for the variation curves of the positive- and negative-contrast stimuli (PN stimuli) used in Chapter 2. The third column of panels, panel C, F, and I, are for the variation curves of the spatial frequency stimuli (SFTC stimuli) used in Chapter 3. The first row of panels is plotted in the log contrast scale, the second row in the log contrast energy scale, the third row in the Fourier-spectrum contrast scale. The red, green, blue, cyan, magenta curves indicate 1, 2, 4, 8, and 16 cpd spatial frequencies or spatial structures stimuli respectively. The offset angle θ is sampled from a set $\{0, \pi/8, \pi/4, 3\pi/8, \pi/2\}$ and the offset distance Δd is ranged between 0 and 0.5 visual degree. The curves with various values of θ are plotted in the same color. All contrast values are normalized.

visual degree. The θ was the offset angle between the x-axis and the line linked two center of stimuli and was sampled from a set $\{0, \pi/8, \pi/4, 3\pi/8, \pi/2\}$.

As showed in Figure 4.9, the variation ranges of contrast of the Gabor stimuli were far more large than those of the PN stimuli and the SFTC stimuli on the log contrast, the log contrast energy, and the Fourier-spectrum contrast while the spatial offset varied in the certain range. The contrast variation of the PN stimuli and the SFTC stimuli were independent with the variation of the direction

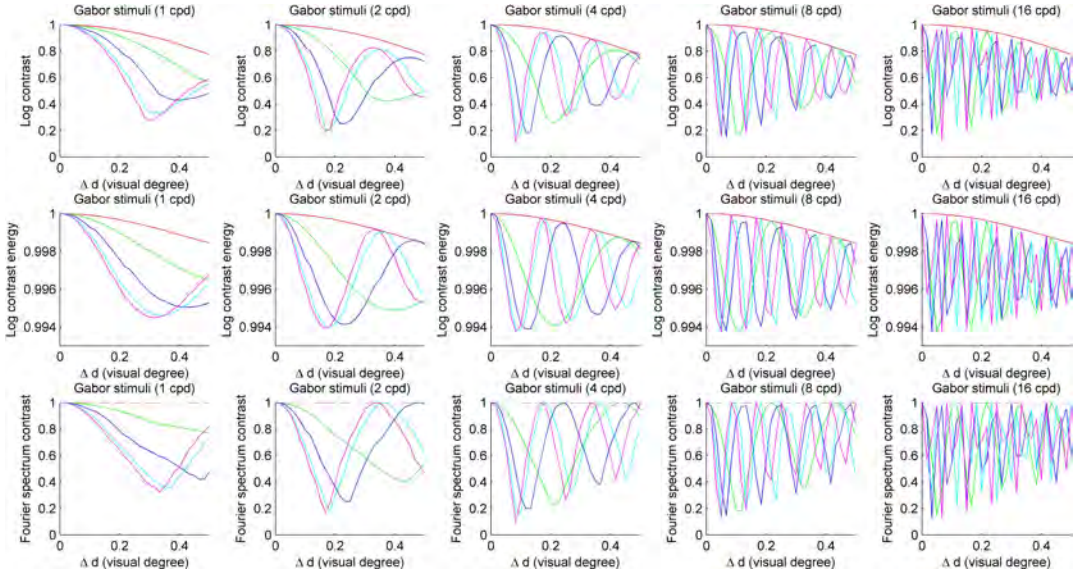

Figure 4.10: The simulation effect of contrast variation for Gabor stimuli. The first, the second, and the third rows of panels are plotted in the log contrast, the log contrast energy, and the Fourier-spectrum contrast respectively. The first column to the fifth column of panels are for spatial frequencies 1, 2, 4, 8, and 16 cpd respectively. The offset angle θ is sampled from a set $\{0, \pi/8, \pi/4, 3\pi/8, \pi/2\}$ which were plotted with the red, green, blue, cyan, magenta curves respectively. The offset distance Δd is ranged between 0 and 0.5 visual degree. All contrast values are normalized.

parameter θ while that of the Gabor stimuli were dependent with the θ. This result indicated that the PN stimuli and SFTC stimuli used in this dissertation are better than the Gabor stimuli in term of the contrast variation caused by the eye movement during the double pulses.

Figure 4.10 showed the simulation effect of contrast variation for the Gabor stimuli only. The irregularity of the contrast variation of the eye movement was depending on the spatial frequency as showing in the figure. Figure 4.11 and Figure 4.12 showed the simulation effect of contrast variation for the PN stimuli and the SFTC stimuli respectively. Those two figures showed relatively regular contrast variation of the eye movement on the spatial frequency (or the spatial

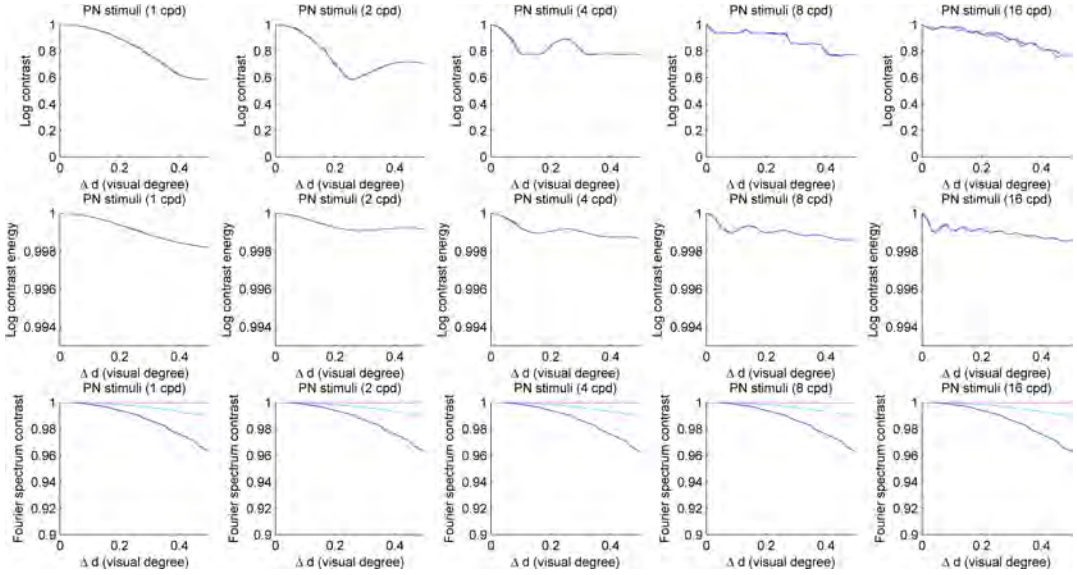

Figure 4.11: The simulation effect of contrast variation for PN stimuli. The first, the second, and the third rows of panels are plotted in the log contrast, the log contrast energy, and the Fourier-spectrum contrast respectively. The first column to the fifth column of panels are for spatial frequencies 1, 2, 4, 8, and 16 cpd respectively. The offset angle θ is sampled from a set $\{0, \pi/8, \pi/4, 3\pi/8, \pi/2\}$ which were plotted with the red, green, blue, cyan, magenta curves respectively. The offset distance Δd is ranged between 0 and 0.5 visual degree. All contrast values are normalized.

structure), the offset angle, and the offset distance.

As showed in Figure 4.9, 4.10, 4.11, and 4.12 the effect of eye movement showed different ways of scaling with various contrast definitions. The log contrast energy and the Fourier-spectrum contrast showed more robust than the log contrast when the spatial frequency, θ, and Δ changed. The reason is that the definitions of the log contrast energy and the Fourier-spectrum contrast are effected by all pixels of the stimuli while the log contrast is only effected by the maximum luminance pixels of the stimuli which is more sensitive with the effect of eye movements. So, the scaling of the log contrast energy and the Fourier-spectrum should be so much less sensitive to detect the possible specially-tuned channels because those

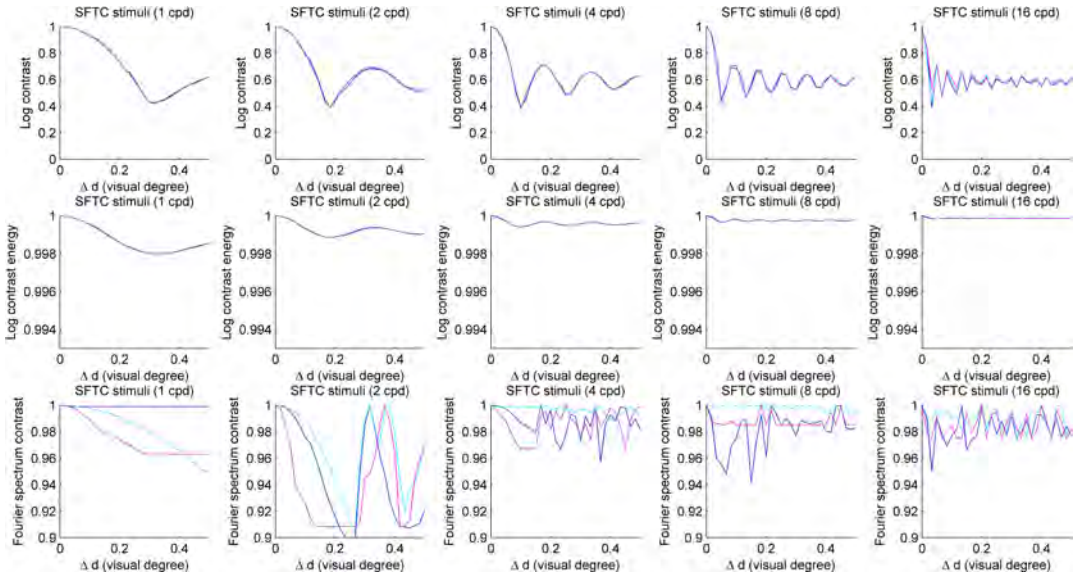

Figure 4.12: The simulation effect of contrast variation for SFTC stimuli. The first, the second, and the third rows of panels are plotted in the log contrast, the log contrast energy, and the Fourier-spectrum contrast respectively. The first column to the fifth column of panels are for spatial frequencies 1, 2, 4, 8, and 16 cpd respectively. The offset angle θ is sampled from a set $\{0, \pi/8, \pi/4, 3\pi/8, \pi/2\}$ which were plotted with the red, green, blue, cyan, magenta curves respectively. The offset distance Δd is ranged between 0 and 0.5 visual degree. All contrast values are normalized.

scaling are too much robust to the change of stimulation.

Above results and analysis showed the PN stimuli and the SFTC stimuli used in this dissertation were better than the Gabor stimuli in simulation effect of contrast variation at eye movements.

The irregularity of the contrast variation of the eye movement was avoided by choosing the PN stimuli and the SFTC stimuli instead of the Gabor stimuli. The log contrast was used to explore the possible spatial-frequency-tuned channels because it was more sensitive to the change of stimulation.

Chapter 5

Conclusions

This chapter summarizes the conclusions which concluded from this dissertation.

5.1 Conclusion about Positive- and Negative-Contrast

Positive- and negative-contrast impulse responses were similar while the sensitivity of positive- and negative-contrast detection was different. This sensitivity difference originates from the summation part rather than the linear filter part of the visual system.

5.2 Conclusion about Spatial-Frequency-Tuned Channels

At least two kinds of spatial-frequency-tuned channels, the lower- and higher-spatial-frequency-tuned channels that dominates the lower spatial frequencies (0,

1, and 2 cpd) and the high spatial frequencies (8 and 16 cpd), respectively, exists in human vision. The lower-spatial-frequency-tuned channel is bandpass and the higher-spatial-frequency-tuned channel is low-pass.

In high possibility, the M- and P-pathways in human visual system dominated the lower spatial frequencies (0, 1, and 2 cpd) and the higher spatial frequencies (8 and 16 cpd), respectively, in the present study.

References

E H Adelson and J R Bergen. Spatiotemporal energy models for the perception of motion. *Journal of the Optical Society of America. A, Optics and Image Science*, 2(2):284–299, February 1985. 66

Stephen J. Anderson and David C. Burr. Spatial and temporal selectivity of the human motion detection system. *Vision Research*, 25(8):1147–1154, January 1985. doi: 10.1016/0042-6989(85)90104-X. 46

E.A. Benardete and E. Kaplan. The dynamics of primate m retinal ganglion cells. *Visual Neuroscience*, 16(2):pp.355–368, 1999. 42

Ethan A. Benardete. *Functional dynamics of primate retinal ganglion cells*. Ph.D. dissertation, The Rockefeller University, 1994. 64

Ethan A. Benardete and Ehud Kaplan. The receptive field of the primate p retinal ganglion cell, i: Linear dynamics. *Visual Neuroscience*, 14(01):169, June 1997. doi: 10.1017/S0952523800008853. 42

Peter J. Bex, N. Brady, R. E. Fredericksen, and R. F. Hess. Energetic motion detection. *Nature*, 378(6558):670–671, December 1995. doi: 10.1038/378670b0. 65

C. Blakemore and F. W. Campbell. On the existence of neurones in the human visual system selectively sensitive to the orientation and size of retinal images. *The Journal of Physiology*, 203(July 1):237–260, 1969. 45, 46

Richard W. Bowen, Joel Pokorny, and Vivianne C. Smith. Sawtooth contrast sensitivity: Decrements have the edge. *Vision Research*, 29(11):1501–1509, January 1989. doi: 10.1016/0042-6989(89)90134-X. 15

Robert M. Boynton, Mitsuo Ikeda, and W.S. Stiles. Interactions among chromatic mechanisms as inferred from positive and negative increment thresholds. *Vision Research*, 4(1-2):87–117, May 1964. doi: 10.1016/0042-6989(64)90035-5. 15

David C. Burr and Concetta Morrone. Temporal impulse response functions for luminance and colour during saccades. *Vision Research*, 36(14):2069–2078, July 1996. doi: 10.1016/0042-6989(95)00282-0. 6

David C. Burr and M. Concetta Morrone. Impulse-response functions for chromatic and achromatic stimuli. *Journal of the Optical Society of America A*, 10 (8):1706, August 1993. doi: 10.1364/JOSAA.10.001706. 5, 7, 8, 22, 53

F. W. Campbell and J. G. Robson. Application of fourier analysis to the visibility of gratings. *The Journal of Physiology*, 197(August 1):551–566, 1968. 45, 46

Dingcai Cao, Andrew J. Zele, and Joel Pokorny. Linking impulse response functions to reaction time: Rod and cone reaction time data and a computational model. *Vision Research*, 47(8):1060–1074, April 2007. doi: 10.1016/j.visres.2006.11.027. 6

E J Chichilnisky and Rachel S Kalmar. Functional asymmetries in ON and OFF

ganglion cells of primate retina. *The Journal of Neuroscience*, 22(7):2737–2747, April 2002. 40, 42

L. de Hann and A. Ferreira. *Extreme Value Theory: An Introduction*. Springer-Verlag, New York, 2006. 70, 71

Russell L. De Valois and Karen K. De Valois. *Spatial Vision*. Number 14 in Oxford Psychology Series. Oxford University Press, USA, August 1990. ISBN 019506657X. 45, 66

Greg D. Field, Jeffrey L. Gauthier, Alexander Sher, Martin Greschner, Timothy A. Machado, Lauren H. Jepson, Jonathon Shlens, Deborah E. Gunning, Keith Mathieson, Wladyslaw Dabrowski, Liam Paninski, Alan M. Litke, and E. J. Chichilnisky. Functional connectivity in the retina at the resolution of photoreceptors. *Nature*, 467(7316):673–677, October 2010. doi: 10.1038/nature09424. 40, 41

Norma Graham and Jacob Nachmias. Detection of grating patterns containing two spatial frequencies: A comparison of single-channel and multiple-channels models. *Vision Research*, 11(3):251–IN4, March 1971. doi: 10.1016/0042-6989(71)90189-1. 46

David M. Green and R. Duncan Luce. Parallel psychometric functions from a set of independent detectors. *Psychological Review*, 82(6):483–486, 1975. doi: 10.1037/0033-295X.82.6.483. 69

Robert M. Herrick. Foveal luminance discrimination as a function of the duration of the decrement or increment in luminance. *Journal of Comparative and Physiological Psychology*, 49(5):437–443, 1956. doi: 10.1037/h0046317. 15

Mitsuo Ikeda. Temporal summation of positive and negative flashes in the visual system. *Journal of the Optical Society of America*, 55(11):1527, November 1965. doi: 10.1364/JOSA.55.001527. 5

E. Kaplan. The m, p, and k pathways of the primate visual system. In *The Visual Neurosciences*. MIT Press, 2004. ISBN 0-262-03308-9. 64

E Kaplan and R M Shapley. The primate retina contains two types of ganglion cells, with high and low contrast sensitivity. *Proceedings of the National Academy of Sciences of the United States of America*, 83(8):2755–2757, April 1986. 64

D. H. Kelly. Visual responses to Time-Dependent stimuli II Single-Channel model of the photopic visual system. *Journal of the Optical Society of America*, 51 (7):747, July 1961. doi: 10.1364/JOSA.51.000747. 5

D. H. Kelly. Theory of flicker and transient responses, I uniform fields. *Journal of the Optical Society of America*, 61(4):537, April 1971. doi: 10.1364/JOSA.61.000537. 5

DH Kelly. Motion and vision. ii. stabilized spatio-temporal threshold surface. *JOSA*, 69(10):1340–1349, 1979. 63, 64

Leonid L. Kontsevich and Christopher W. Tyler. Bayesian adaptive estimation of psychometric slope and threshold. *Vision Research*, 39(16):2729–2737, August 1999. doi: 10.1016/S0042-6989(98)00285-5. 10, 13, 21, 52

Leonid L. Kontsevich and Christopher W. Tyler. A simpler structure for local

spatial channels revealed by sustained perifoveal stimuli. *Journal of Vision*, 13 (1), 2013. doi: 10.1167/13.1.22. 65

Jan Kremers, Barry B. Lee, Joel Pokorny, and Vivianne C. Smith. Responses of macaque ganglion cells and human observers to compound periodic waveforms. *Vision Research*, 33(14):1997–2011, September 1993. doi: 10.1016/0042-6989(93)90023-P. 41, 42

J. Kruger and B. Fischer. Symmetry between the visual b- and d-systems and equivalence of center and surround: Studies of light increment and decrement in retinal and geniculate neurons of the cat. *Biological Cybernetics*, 20(3-4): 223–235, 1975. doi: 10.1007/BF00342642. 41

BB Lee, PR Martin, and A. Valberg. Amplitude and phase of responses of macaque retinal ganglion cells to flickering stimuli. *The Journal of physiology*, 414(1):245–263, 1989. 63

A Logvinenko. Method of quadratic approximation: A new approach to identification of analysers and channels in human vision. *Journal of Mathematical Psychology*, 47(5-6):495–506, December 2003. doi: 10.1016/S0022-2496(03)00048-8. 46

M. J. Morgan. Spatial filtering precedes motion detection. *Nature*, 355(6358): 344–346, January 1992. doi: 10.1038/355344a0. 65

M.J. Morgan and G. Mather. Mostion discrimination in two-frame sequences with differing spatial frequency content. *Vision Research*, 34(2):197–208, January 1994. doi: 10.1016/0042-6989(94)90332-8. 65

Shinji Nishimoto, Miki Arai, and Izumi Ohzawa. Accuracy of subspace mapping of spatiotemporal frequency domain visual receptive fields. *Journal of Neurophysiology*, 93(6):3524–3536, June 2005. doi: 10.1152/jn.01169.2004. PMID: 15647396. 46

Shinji Nishimoto, Tsugitaka Ishida, and Izumi Ohzawa. Receptive field properties of neurons in the early visual cortex revealed by local spectral reverse correlation. *The Journal of Neuroscience*, 26(12):3269–3280, March 2006. doi: 10.1523/JNEUROSCI.4558-05.2006. 46

C. Pandarinath, J. D. Victor, and S. Nirenberg. Symmetry breakdown in the ON and OFF pathways of the retina at night: Functional implications. *Journal of Neuroscience*, 30:10006–10014, July 2010. doi: 10.1523/JNEUROSCI.5616-09.2010. 42

A. S. Patel and R. W. Jones. Increment and decrement visual thresholds. *Journal of the Optical Society of America*, 58(5):696, May 1968. doi: 10.1364/JOSA.58.000696. 15

N. Prins and F. A. A. Kingdom. Palamedes: Matlab routines for analyzing psychophysical data, 2009. URL `http://www.palamedestoolbox.org/`. 10, 21, 52

C. Rashbass. The visibility of transient changes of luminance. *The Journal of Physiology*, 210(1):165–186, 1970. 15

Murray B. Sachs, Jacob Nachmias, and John G. Robson. Spatial-Frequency channels in human vision. *Journal of the Optical Society of America*, 61(9):1176, September 1971. doi: 10.1364/JOSA.61.001176. 46

Keizo Shinomori and John S. Werner. Senescence of the temporal impulse response to a luminous pulse. *Vision Research*, 43(6):617–627, March 2003. doi: 10.1016/S0042-6989(03)00009-9. 6, 8, 22, 36, 42, 53

Keizo Shinomori and John S. Werner. Impulse response of an s-cone pathway in the aging visual system. *Journal of the Optical Society of America A*, 23(7): 1570, 2006. doi: 10.1364/JOSAA.23.001570. 6

Keizo Shinomori and John S. Werner. The impulse response of s-cone pathways in detection of increments and decrements. *Visual Neuroscience*, 25(03):341–347, March 2008. doi: 10.1017/S0952523808080218. 6

Keizo Shinomori and John S. Werner. Aging of human short-wave cone pathways. *Proceedings of the National Academy of Sciences*, 109(33):13422–13427, 2012. doi: 10.1073/pnas.1119770109. 6

A. D. Short. Decremental and incremental visual thresholds. *The Journal of Physiology*, 185(3):646–654, 1966. 15

V.C. Smith, BB Lee, J. Pokorny, PR Martin, and A. Valberg. Responses of macaque ganglion cells to the relative phase of heterochromatically modulated lights. *The Journal of Physiology*, 458(1):191–221, 1992. 63

David G. Stork and David S. Falk. Temporal impulse responses from flicker sensitivities. *Journal of the Optical Society of America A*, 4(6):1130, June 1987. doi: 10.1364/JOSAA.4.001130. 5

Keiji Uchikawa and Mitsuo Ikeda. Temporal integration of chromatic double pulses for detection of equal-luminance wavelength changes. *Journal of the Op-*

tical Society of America A, 3(12):2109, December 1986. doi: 10.1364/JOSAA.3.002109. 5

Keiji Uchikawa and Tatsuya Yoshizawa. Temporal responses to chromatic and achromatic change inferred from temporal double-pulse integration. *Journal of the Optical Society of America A*, 10(8):1697, August 1993. doi: 10.1364/JOSAA.10.001697. 5

A. B. Watson and A. J. Ahumada. A standard model for foveal detection of spatial contrast. *Journal of Vision*, 5(9):717–740, October 2005. doi: 10.1167/5.9.6. 3, 46

A B Watson and Jr Ahumada, A J. Model of human visual-motion sensing. *Journal of the Optical Society of America. A, Optics and Image Science*, 2(2): 322–341, February 1985. 65

A.B. Watson. Temporal sensitivity. In *Handbook of Perception and Human Performance*. New York: Wiley, 1986. 2, 3, 7, 8, 22, 34, 40, 53

Andrew B. Watson. Probability summation over time. *Vision Research*, 19(5): 515–522, January 1979. doi: 10.1016/0042-6989(79)90136-6. 7, 22, 53, 69

Andrew B. Watson and Jacob Nachmias. Patterns of temporal interaction in the detection of gratings. *Vision Research*, 17(8):893–902, January 1977. doi: 10.1016/0042-6989(77)90063-3. 15

Andrew B. Watson, H. B. Barlow, and John G. Robson. What does the eye see best? *Nature*, 302(5907):419–422, March 1983. doi: 10.1038/302419a0. 18

W. Weibull. A statistical distribution function of wide applicability. *Journal of applied mechanics*, 19:292–297, 1951. 69, 71

H Wilson, D Mcfarlane, and G Phillips. Spatial frequency tuning of orientation selective units estimated by oblique masking. *Vision Research*, 23(9):873–882, 1983. doi: 10.1016/0042-6989(83)90055-X. 46

H. R. Wilson and F. Wilkinson. Spatial channels in vision and spatial pooling. In *The Visual Neurosciences*. MIT Press, 2004. 46

Hugh R. Wilson and James R. Bergen. A four mechanism model for threshold spatial vision. *Vision Research*, 19(1):19–32, January 1979. doi: 10.1016/0042-6989(79)90117-2. 46

Chun-I Yeh, Dajun Xing, and Robert M Shapley. "Black" responses dominate macaque primary visual cortex v1. *The Journal of Neuroscience*, 29(38):11753–11760, September 2009. doi: 10.1523/JNEUROSCI.1991-09.2009. 41

Publications

Publications on Journals

Lin Shi, Keizo Shinomori (2013). Amplitude difference and similar time course of impulse responses in positive- and negative-contrast detection. **Vision Research**, 77(25), 2131. **SCI** indexed, **impact factor: 2.5**, http://dx.doi.org/10.1016/j.visres.2012.11.006

Keizo Shinomori, Lin Shi, Impulse responses of the possible spatial-frequency-tuned channels (to be submitted)

Publications on Conference

Lin Shi, Keizo Shinomori, Luminous impulse response of positive- and negative-contrast stimuli in different spatial frequencies, i-Perception, 2(4) 370, DOI:10.1068/ic370, 2011

Lin Shi, Keizo Shinomori, Influences of spatial frequency to luminous impulse response for positive and negative flashes, International Workshop on Information Technology, 15, 2010

Lin Shi, Keizo Shinomori, Chinese text entry method using reduced number of strokes, International Workshop on Information Technology, 36, 2009

Acknowledgements

I would like to acknowledge my adviser Professor Keizo Shinomori. He is an very precise and very smart example in my academic career. His rigorous approach in scientific research is the best reason to be advised by him. Following him, I stepped into the interesting vision psychophysics field and learned how to do basic scientific research.

I would like to acknowledge Professor Shuoyu Wang, Professor Hiroaki Shigemasu, Professor Mamoru Okada, and Dr. Hiroshi Kadota for their kind help and advices to my academic career.

President Taketo Sakuma for his kind care when I was in trouble.

Professor Mikiko Ban for her kindness and help extended to my family in their visit to Japan. Her kindness is my best memory in Japan!

Professor Zhiqing Ding, Professor Akimitsu Hata, Professor Tsunemi Watanabe, Professor Chaoyang Li, Mrs. Fukudome, Mr. Yoshida, Mrs. Fujii, Mrs. Yoshida, and Mrs. Mari for their kind help.

I also would like to acknowledge my wife for her love and English correction of my dissertation, without her support, my doctoral course would not have been possible. For my angelic daughter, I am sorry I was not with you in three years.